NONLINEAR ELECTROKINETIC TRANSPORT AND ITS APPLICATIONS UNDER
COMBINED AC AND DC FIELDS IN MICRO/NANOFLUIDIC INTERFACE DEVICES

BY

VISHAL VENKATA RAGHAVE NANDIGANA

THESIS

Submitted in partial fulfillment of the requirements
for the degree of Master of Science in Mechanical Engineering
in the Graduate College of the
University of Illinois at Urbana-Champaign, 2011

Urbana, Illinois

Adviser:

Professor Narayana R. Aluru

Abstract

The integration of micro/nanofluidic devices led to many interesting phenomena and one of the most important and complex phenomenon among them is concentration polarization. In this thesis, we provide new physical insights in micro/nanofluidic interface devices on the application of AC and DC electric fields. By performing detailed numerical simulations based on coupled Poisson, Nernst−Planck, and incompressible Navier−Stokes equations, we discuss the electrokinetic transport and other hydrodynamic effects under the application of combined AC and DC electric fields for different nondimensional EDL thickness and nanochannel wall surface charge density. We understand that for a highly ion−selective nanochannel, the application of combined AC/DC electric field, at amplitudes greater than the DC voltage and at low Strouhal number, results in large dual concentration polarization regions (with unequal lengths) at both the micro/nanofluidic interfaces due to large and unequal voltage drops at these junctions. The highly nonlinear potential distribution gives rise to an electric field and body force that changes the electrokinetic fluid velocity from that obtained on the application of only a DC source. With the understanding of nonlinear electrokinetic transport under combined AC/DC fields, we propose a novel technique of increasing the product concentration of an enzymatic reaction inside the nanofluidic channel.

Acknowledgments

First of all I would like to extend my gratitude towards Prof N. R. Aluru for his continuous encouragement, guidance, and complete academic and financial support. My interactions with him helped me develop a penchant towards understanding the fundamental fluid dynamics in confined environments, and apply my knowledge in this challenging field. I hope our interactions would lead to further good research in this exciting field in the future.

Special thanks to Dr. Xiaozhong Jin, post Doctoral fellow in Prof Aluru's group for his kind support and valuable suggestions.

I would also like to thank all my colleagues whose valuable suggestions and interactions helped me in many ways during the course of my research.

Finally, I would like to express my sincere appreciation for the continuous love and support of my parents, Dr. Krishna Mohan Nandigana, who is always my inspiration in all walks of my life and Mrs. Lakshmi Nandigana. My brother, Santosh Kumar Nandigana deserves a special mention for his moral support.

Table of Contents

Chapter 1

Introduction

Over the last couple of decades, the advancements in micromanufacturing technology have paved way for the development of lab−on−a−chip devices. These miniaturized microfluidic devices have found extensive applications in biological sensing, mixing, drug delivery, pumping fluids, separation of chemical species etc. [1, 2, 3, 4], where the fluid transport processes occur at significantly smaller time and length scales compared to their macroscopic counterparts. The reduction of the sample consumption, efficient control of the convective transport and improved heat transfer were the primary motivation behind developing such miniaturized systems [5]. Further, the simplistic design of such devices, aids in massive parallelization, thus enabling them to automate processes in chemical, biological and fluidic systems [6].

Latest advancements in the fabrication technology [7, 8, 9] have motivated researchers around the globe to investigate the transport phenomenon in channel sizes of the order of few hundreds of nanometers. The study and application of fluid flow at these confined length scales is often referred as "Nanofluidics". The large surface−area−to−volume ratio in nanofluidic systems has led to many new physical phenomenon that are not observed at the micro scales. The influence of nanochannel surface charge, its size, shape and the strength of the electrolyte on the ionic transport are some of the fundamental studies which has triggered a lot of attention in the recent past [10, 11, 12]. In order to understand the transport phenomenon in nanofluidic channels, it is important to understand the properties associated with such systems [13].

In the following section, we present few distinct properties of micro and nanofluidic systems which influence their transport.

1.1 Electrostatics in liquids

A solid in contact with an aqueous solution acquires a surface charge (σ_s) due to the dissociation of ionizable groups on the solid walls along with the specific adsorption of ions (in the solution) on to the walls [14]. The negative or positive surface charge density depends on the number and type of acid and basic groups present in the solution which is given by $\sigma_s = \sum_i \frac{q_i}{A}$, where $q_i = z_i e$ is the net charge of ion i, z_i is the valency of ion i, e is the electron charge and A is the surface area. The surface charges result in the electrostatic force, which typically describes the long$-$range interaction between the molecules and the surfaces in liquids. At small distances, van der Waals force leads to attraction between two molecules. The interplay between van der Waals and electrostatic force is elaborately discussed in the Derjaguin-Landau-Verwey-Overbeek (DLVO) theory [15], which describes most of the colloidal stability. The electrostatic force has high dependence on the ionic strength of the electrolyte, while, van der Waals force is generally insensitive to the changes in the electrolyte concentration.

1.2 Electrical Double Layer (EDL)

The fixed surface charge on the solid surface in contact with the liquid develops a region of counterions (ions with charges opposite to the solid surface) in the liquid to maintain the electroneutrality at the solid$-$liquid interface. This screening region is denoted as the Electrical Double Layer (EDL) or Debye Length (DL). Some of the counterions present in the EDL region are bound to the surface while others are free to move. The layer where the ions get strongly attracted towards the channel surface due to the electrostatic force is called the inner layer with potential (ψ_i) and have a typical thickness of one ion diameter. The second layer is defined by the outer Helmholtz plane with potential (ψ_d). The outermost and third layer is the diffuse layer, composed of mobile co$-$ions and counterions, which consists of the slip plane with ζ potential. The outer Helmholtz plane and the slip plane are close

to each other and hence the potential ψ_d is typically approximated by the ζ potential. The ζ potential can be experimentally determined and is found to depend on the pH and ionic strength of the solution. Fig. 1.1 displays the structure of EDL with different layers. The EDL thickness (λ_D) is given by [16]:

$$\lambda_D = \left(\frac{\epsilon_o \epsilon_r RT}{F^2 \sum_{i=1}^{m} z_i^2 c_0} \right)^{1/2} \tag{1.1}$$

where, F is Faraday's constant, z_i is the valence of ionic species i, c_0 is the bulk concentration of the electrolyte solution, m is the number of ionic species, ϵ_0 is the permittivity of free space, ϵ_r is the relative permittivity of the medium, R is the universal gas constant and T is the absolute temperature. The EDL thickness depends inversely to the square root of the ionic strength of the electrolyte. For a symmetrical electrolyte like KCl, with a decrease in the ionic strength from $1\,mM$ to $0.1\,mM$, the EDL thickness increases from $10\,nm$ to $30\,nm$.

Stern, proved that assuming the electrolyte ions as point charges and the solvent as a structure less dielectric of constant permittivity were quite unsatisfactory. Hence, he introduced another layer viz. Stern layer between the inner and the outer Helmholtz plane, in which the charge and potential distribution are assumed to be linear, and a diffuse layer away from the wall was modeled using the Gouy−Chapman theory [17]. In this thesis, we neglect the potentials developed in the stern layer and use continuum models to capture the potential across the entire micro and nanochannel. A detailed discussion on the theoretical modeling is provided in the next chapter.

We would like to point out that the electrostatic interactions play a significant role in the transport of confined micro/nanofluidic devices and we discuss the various electrokinetic transport mechanisms in the next section.
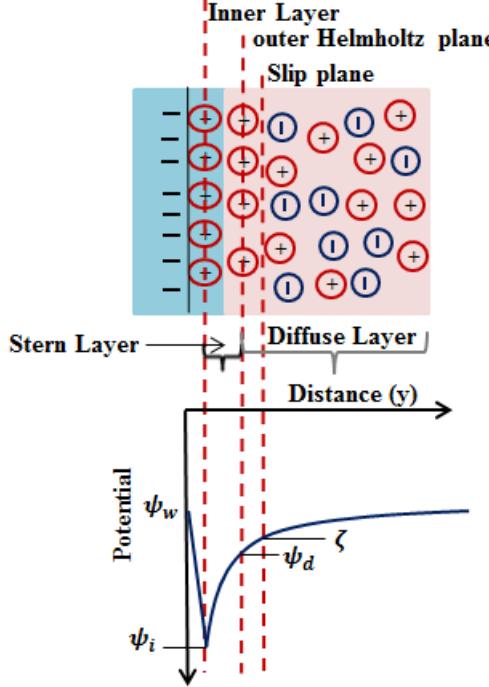
Figure 1.1: Structure of EDL indicating different layers. The first layer represents the inner Helmholtz layer with potential (ψ_i), the next layer is the outer Helmholtz layer with potential (ψ_d) and the final layer is the diffusive layer consisting of slip plane with (ζ) potential. ψ_w is the surface potential of the negatively charged solid.

1.3 Electrokinetic flows

The fluid transport in micro and nanochannels is predominantly achieved by the application of external electric fields and the study of such transport phenomenon is often referred as "Electrokinetics". The electric fields interact with the EDL to create an electrostatic body force on the liquid. The liquid is driven by a viscous drag via the shear stresses concentrated in the EDL region. The application of electric fields inside micro and nanofluidic devices aids better control when compared to using pressure driven techniques [18]. The electric fields help in overcoming the high pressures needed to transport the fluid at such length scales [8] as the pressure follows a power−law relation with respect to the height of the channel [19]. Electrokinetic flows include *electroosmosis, electrophoresis, dielectrophoresis and electrorotation*. The first two theories play a predominant role in micro and nanofluidic

transport and is explained in this section.

Electroosmosis is the bulk motion of a fluid containing charged species under the action of an applied electric field adjacent to the negatively/positively charged channel walls [20]. If the walls of the channel are negatively charged, a layer of cations builds-up near the surface creating an electrical double layer of ions and a potential difference as discussed in the previous section. When an electric field is applied, this layer of positive charge is attracted towards the cathode, resulting in the bulk flow of the liquid [21].

In microfluidic systems, the liquid velocity is zero at the slip plane (i.e at the beginning of the diffuse layer), increases to a maximum value at distances equal to the EDL thickness and remains constant at high ionic strength of the solution, i.e., in the bulk region of the channel. As the EDL thickness in these channels is much smaller compared to their height ($\frac{h}{\lambda_D} \gg 1$), the fluid follows a plug like flow characteristics. The bulk flow of the fluid (u_{eo}) driven by electric field is approximated [22] based on the Helmholtz - Smoluchowski Equation (1.2).

$$u_{eo} = -\frac{\epsilon_r \epsilon_0 \zeta \mathbf{E}_x}{\mu} \tag{1.2}$$

where μ is the viscosity of the fluid, $\mathbf{E}_x$ is the applied axial electric field. In the case of nanofluidic channels, the electrical double layer spans much of the diameter or channel height ($\frac{h}{\lambda_D} \approx 1$) leading to many interesting transport phenomenon compared to its microscopic counterpart. The fluid velocity no longer follows a plug like flow characteristics but follows a Poiseuille like (parabolic) characteristics as the electrokinetic body force is not just confined to the thin layer adjacent to the channel surface. The flow characteristics in both micro and nanoscale systems is depicted in Fig. 1.2(a) and Fig. 1.2(b), respectively. Equation (1.3) describes the velocity distribution in systems when λ_D becomes comparable to the channel height h.

$$u_{eo} = -\frac{\epsilon_r \epsilon_0 \zeta \mathbf{E}_x}{\mu} \left(1 - \frac{\psi(z)}{\zeta} \right) \tag{1.3}$$

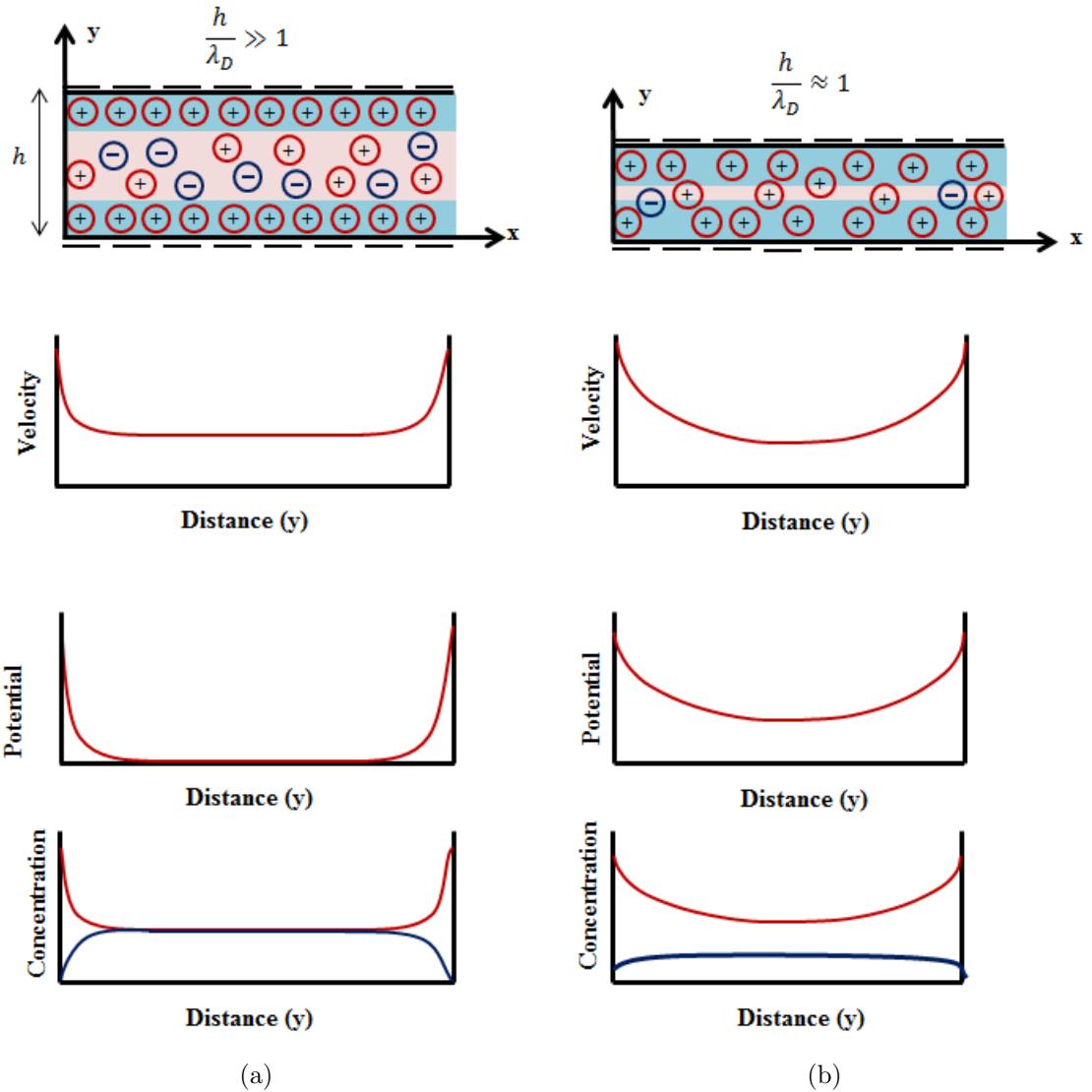where $\psi(z)$ is the potential distribution across the channel.

Figure 1.2: Schematic illustration of EDL physics in (a) microchannels ($\frac{h}{\lambda_D} \gg 1$) and (b) nanochannels ($\frac{h}{\lambda_D} \approx 1$). In thin EDL channels (a), the electric potential falls to zero (indicating bulk region having equal coions and counterions concentration) and the fluid velocity follows plug like flow characteristics. In thick EDL channels (b), the potential doesn't reach zero resulting in ion−selective systems with concentration of counterions greater than coions and the fluid velocity follows a Poiseulle like parabolic distribution.

The other important electrokinetic phenomenon used to control motion of particles and molecules in micro and nanofluidic systems is Electrophoresis.

Electrophoresis is the motion of dispersed particles relative to a fluid under the influence of a spatially uniform electric field. This electrokinetic phenomenon was first observed in

1807 by Reuss [23] who noticed that the application of a constant electric field caused clay particles dispersed in water to migrate. This phenomenon is often considered as the converse of electroosmosis, as the liquid is considered fixed while, the particle moves in the opposite direction relative to the solution. Elaborate details of this mechanism are given below. When a charged particle is placed in the aqueous solution, counterions screen the charges of the molecule to maintain overall electroneutrality. Under the action of an applied electric field, the charged particle moves as the ions in the EDL are not fixed to the surface. The counterions in the EDL would move in the direction opposite to the charged particles (if it were unscreened), leading to the fluid motion around the particle (electroosmosis). In the case of low Reynolds number and moderate axial electric field strength $\mathbf{E}_x$, the speed of a particle, u_{ep} is simply proportional to the applied field and is influenced by the viscosity of the solution:

$$u_{ep} = \mu_{ep}\mathbf{E}_x \tag{1.4}$$

where $\mu_{ep} = \frac{\epsilon_r\epsilon_0\zeta}{\mu}$ is the electrophoretic mobility. The above equation was found to be valid only for thin EDL when the particle radius is much greater than the EDL. In cases of thick EDL, the electrophoretic mobility is given by Equation (1.5) as predicted by Hückel [24]. They can be used for studying the electrostatic interactions in nanoparticles and colloidal systems.

$$\mu_{ep} = \frac{2\epsilon_r\epsilon_0\zeta}{3\mu}. \tag{1.5}$$

1.4   Ion selectivity of nanochannels

In the previous section, we have addressed an important difference between the microfluidic and nanofluidic electroosmotic transport. In this section, we highlight the difference in the ionic transport between the two systems. As the EDL becomes comparable to the nanochannel height ($\frac{h}{\lambda_D} \approx 1$), the local electrical potential, which decreases from the channel

7

wall towards the center of the channel, doesn't reach the bulk value (unlike in microfluidic systems). The presence of electrical potential inside the whole channel increases the concentration of the counterions and excludes the coions as shown in Fig. 1.2. The nanochannel as a whole becomes an ion−selective membrane. At electrochemical equilibrium, the concentration (both coion and counterion) and the electrical potential inside the nanochannel can be obtained using the Donnan equilibrium theory [3]. Along with the EDL, the surface charge also plays a prominent role in controlling the ion transport inside the nanofluidic systems [11].

In contrast to the nanofluidic systems, the counterionic mobile space charge is confined to very thin layer adjacent to the surface of the microchannel as the EDL thickness is much smaller compared to their height ($\frac{h}{\lambda_D} \gg 1$). Thus, the region away from the surface is essentially quasi−electroneutral (i.e, both co−ions and counter−ions are present away from the surface). Consequently, the microfluidic channel is not ion−selective as illustrated in Fig. 1.2. Similar ion−selective phenomenon was also observed in the intraparticle and intraskeloton mesopores of particulate [25, 26] and in membrane science [27].

As the electrokinetic and ion transport phenomenon in nanofluidic devices is different in comparison to its microscopic counterpart, the integration of these two devices paves way to a much complex physics. In this thesis, we study the electrokinetic transport on the hybrid micro/nanofluidic interconnect devices under different electric fields. We primarily focus on the nonlinear electrokinetic effects that are observed under the action of strong DC electric fields and also investigate the effect of combined AC and DC fields on the electrokinetic transport and other hydrodynamic properties. The complex physics observed at the interfaces under these electric fields would be thoroughly investigated.

Chapter 2

Theoretical modeling

2.1   Introduction

In this chapter, we discuss a complete set of equations for modeling the electrokinetic transport and to account for the EDL effects which were discussed in the previous chapter. Several studies in the past have shown that the continuum theory can accurately describe the electrokinetic transport for dimensions larger than several nanometers [28, 29, 30]. In the current thesis, as the smallest dimension considered for the numerical study is 10 nm, continuum theory has been used to understand the electrokinetic transport phenomenon. It is important to note that all these theories would breakdown at smaller channel sizes due to the collisions between the molecules and the walls leading to layering effects near the walls [31]. At these scales, the transport phenomenon is modeled using molecular−dynamics simulations [32], where a set of molecules with initial random positions are assumed and initial random velocities are assigned corresponding to the Boltzmann distribution and Newton's laws of motion are applied to evaluate the atomic positions with respect to time. As these methods take large computational time, to overcome them several techniques, such as dissipative particle dynamics [33], density−functional theory [34] and empirical potential based quasicontinuum theory [35, 36] are developed.

2.2   Nonlinear electrokinetic model

To understand the complete nonlinear ionic and electrokinetic transport, space charge model developed by Gross et al. [37] and its extension by Wang et al. [38] is implemented. The

model solves the classical Poisson−Nernst−Planck (PNP) equations (which describes the electrochemical transport) and the incompressible Navier−Stokes equation along with the continuity equation to describe the movement of the fluid flow. These coupled system of equations are more intensive, mathematically complicated and computationally expensive. Though many linearized approximations were proposed to this model to study the ion−transport [39, 40], the governing equations of the complete nonlinear space charge model will be discussed in this chapter.

2.2.1 Ionic species transport

In electrokinetic flows, the total flux is contributed by three terms: a diffusive component resulting from the concentration gradient, an electrophoretic component arising due to the potential gradient and a convective component originating from the fluid flow. The total flux of each species in the solution is given by,

$$\mathbf{\Gamma}_i = -D_i \nabla c_i - \Omega_i z_i F c_i \nabla \phi + c_i \mathbf{u} \tag{2.1}$$

where $\mathbf{\Gamma}_i$ is the flux vector, F is Faraday's constant, z_i is the valence, D_i is the diffusion coefficient, Ω_i is the ionic mobility, c_i is the concentration of the ith species, $\mathbf{u}$ is the velocity vector of the fluid flow and ϕ is the electrical potential. Note that the ionic mobility is related to the diffusion coefficient by Einstein's relation [22], $\Omega_i = \frac{D_i}{RT}$, where R is the ideal gas constant and T is the thermodynamic temperature. The mass transfer of each buffer species is given by,

$$\frac{\partial c_i}{\partial t} = -\nabla \cdot \mathbf{\Gamma}_i \tag{2.2}$$

The individual ionic current through the channel is calculated by integrating their respective fluxes over the cross−sectional area, i.e.,

$$\mathbf{I}_i = \int_S z_i F \mathbf{\Gamma}_i \, dS \tag{2.3}$$

and the total ionic current through the channel is calculated as,

$$\mathbf{I} = \int_S \sum_i z_i F \mathbf{\Gamma}_i \, dS \tag{2.4}$$

where S is the cross−sectional area of the channel.

2.2.2 Electrostatic potential interaction

The electrical potential distribution is calculated by solving the Poisson's equation,

$$\nabla \cdot \mathbf{D} = \rho_e \tag{2.5}$$

where ρ_e is the net space charge density of the ions and $\mathbf{D}$ is the electric displacement field which are defined by Equation (2.6) and Equation (2.7), respectively.

$$\rho_e = F \left(\sum_{i=1}^m z_i c_i \right) \tag{2.6}$$

where m is the total number of species considered in the system.

$$\mathbf{D} = \epsilon_0 \mathbf{E} + \mathbf{P} \tag{2.7}$$

where $\mathbf{P}$ is the electric polarization, $\mathbf{E}$ is the applied electric field and ϵ_0 is the permittivity of free space. The electric polarization is directly proportional to the electric field when the electrolyte is assumed to be linear, isotropic and homogeneous with respect to its electric

properties.

$$\mathbf{P} = \epsilon_0 \chi_e \mathbf{E} \tag{2.8}$$

where χ_e is the constant electric susceptibility. Thus, the electric displacement is directly proportional to the electric field ($\mathbf{E}$) and the electric field is given by the gradient of an electric scalar potential ϕ under the electric quasi statics assumption.

$$E = -\nabla\phi \tag{2.9}$$

The electric displacement finally reduces to,

$$\mathbf{D} = (1 + \chi_e)\,\epsilon_0\mathbf{E} = \epsilon_r\epsilon_0\mathbf{E} = -\epsilon_r\epsilon_0\nabla\phi \tag{2.10}$$

where ϵ_r is the relative permittivity of the medium (here water is considered as the medium; $\epsilon_r = 80$). Substituting the above expression in Equation (2.5) simplifies Poisson's equation for an isotropic electrolyte to,

$$\nabla \cdot (\epsilon_r \nabla\phi) = -\frac{\rho_e}{\epsilon_0} \tag{2.11}$$

Equation (2.11), Equation (2.2) and Equation (2.1) are the classical Poisson$-$Nernst$-$Planck (PNP) equations, which describe the electrochemical transport. The continuity and the momentum conservation equations are considered, to describe the movement of the fluid flow through the channel.

2.2.3   Continuity equation

The mass conservation is obtained by solving the continuity equation [20]

$$\frac{\partial\rho}{\partial t} + \nabla \cdot (\rho\mathbf{u}) = 0 \tag{2.12}$$

where ρ is the density of the electrolyte buffer and $\mathbf{u}$ is the velocity vector of the fluid. In our system, the fluid is assumed to be incompressible and Equation (2.12) reduces to

$$\nabla \cdot \mathbf{u} = 0 \tag{2.13}$$

2.2.4 Momentum conservation

The conservation of momentum is given by the incompressible Navier−Stokes (NS) equation

$$\rho \left(\frac{\partial \mathbf{u}}{\partial t} + \mathbf{u} \cdot \nabla \mathbf{u} \right) = -\nabla p + \mu \nabla^2 \mathbf{u} + \rho_e \mathbf{E} \tag{2.14}$$

where $\mathbf{u}$ is the velocity vector, p is the pressure, ρ and μ are the density and the viscosity of the fluid, respectively, and $\mathbf{E} = -\nabla \phi$ is the electric field. $\rho_e \mathbf{E}$ is the electrostatic body force acting on the fluid due to the space charge density and the applied electric field.

2.3 Boundary Conditions

2.3.1 Electrostatic boundary condition

As the walls of the channel are typically charged, applying the charge conservation at the walls lead to the following electrostatic boundary condition.

$$\mathbf{n}_w \cdot \nabla \phi = \frac{\sigma}{\epsilon_0 \epsilon_r} \tag{2.15}$$

where σ represents the surface charge density on the walls of the channel and $\mathbf{n}_w$ denotes the unit normal vector (pointing outwards) to the channel surface.

2.3.2   Flux boundary condition

The normal flux of each ion is assumed to be zero [41] on the channel walls so that there is no leakage of current and is given by

$$\mathbf{n}_w \cdot \boldsymbol{\Gamma}_i = 0 \tag{2.16}$$

2.3.3   Hydrodynamic boundary condition

The fluid velocities on the wall surfaces are assumed to be subjected to non−slip boundary conditions and also the gradients of pressure are assumed to be zero on the walls, i.e.,

$$\mathbf{u} = 0, \quad \mathbf{n}_w \cdot \nabla p = 0 \tag{2.17}$$

The complete nonlinear electrokinetic model with the necessary boundary conditions are used to predict the nonlinear electrokinetic transport under the application of different electric fields in micro/nanofluidic devices. The flow characteristics under large DC electric fields are discussed in detail in chapter 4, while the nonlinear electrokinetic transport under combined AC and DC electric fields would be discussed in chapter 5. The coupled PNP and Navier−Stokes equations are numerically solved using the finite volume method in Open-FOAM [42](Open Field Operation and Manipulation). The numerical implementation and the validation of the model is discussed in the next chapter.

Chapter 3

Numerical implementation and code validation

3.1 Methodology

A brief description on the finite volume method and the features of OpenFOAM used for modeling the PNP and Navier−Stokes equations are discussed in this section. In finite volume method, the volume integrals in the PDE containing a divergence term are converted to surface integrals using the divergence theorem [43]. At the surface of each finite volume, these divergence terms are evaluated as fluxes. By finite volume, we refer to a small control volume surrounding each nodal point on a mesh geometry. The primary advantage of this method is that it ensures conservation of all equations, as it evaluates fluxes which are conserved in a given volume. Along with this, it can easily be formulated even for unstructured meshes. The method also provides different spatial and temporal discretization techniques and schemes. A detailed discussion of the schemes can be found in Ref [43, 44]. In the current thesis, the convective terms in the PNP equations are discretized using second order bounded NVD schemes [45] and all the Laplacian terms are discretized using second order central differencing scheme. The Navier−Stokes equations are solved using SIMPLE algorithm [43].

3.2 An outlook on OpenFOAM

OpenFOAM (OpenField Operation and Manipulation) is an open source, finite volume based CFD software (produced by OpenCFD Ltd.). The software offers great flexibility in dealing with complex problems ranging from complex turbulent flows and fluid−structure interac-

tions to solid dynamics and electrohydrodynamics. As OpenFOAM is an object−oriented code written in C++, it allows for straightforward implementation of new models along with an efficient incorporation of the existing solvers. Here, we implement the solvers for modeling PNP equations. In order to solve a system of PDEs, separate matrix equations are constructed using finite volume schemes and is solved using iterative techniques. In the current thesis, we use preconditioned bi−conjugate gradient solver (PBiCG) for asymmetric matrices and preconditioned conjugate gradient solver (PCG) is used for symmetric matrices. The solver implementation structure in OpenFOAM is highlighted below.

3.2.1   Code Structure

Among its many other advantages discussed earlier, the biggest merit of using OpenFOAM is that the top level codes can be written directly as equations being solved. For instance, the equation

$$\frac{\partial \rho \mathbf{u}}{\partial t} + \nabla \cdot \rho \mathbf{u}\mathbf{u} - \nabla \cdot \mu \nabla \mathbf{u} = -\nabla p \tag{3.1}$$

is represented in OpenFOAM as:

solve

(

fvm::ddt(rho, u)

+ fvm::div(phi, u)

- fvm::laplacian(mu, u)

==

- fvc::grad(p)

);

The flexibility in coding these equations provides greater freedom to modify and implement new solvers.

3.3 Validation

In order to check the accuracy of the numerical solver developed using OpenFOAM, we compared our results with the data published in [28]. We further calibrated the accuracy of the ionic concentration distribution inside the charged nanochannel by comparing with the overall electroneutrality condition.

3.3.1 Simulation model

Considering a $2-$D geometry similar to Daiguji et al. [28] (see Fig. 3.1), we compare the ionic transport of KCl electrolyte solution inside charged nanofluidic device. A $2-$D Poisson$-$Nernst$-$Planck model discussed in chapter 2 is used in the present analysis.
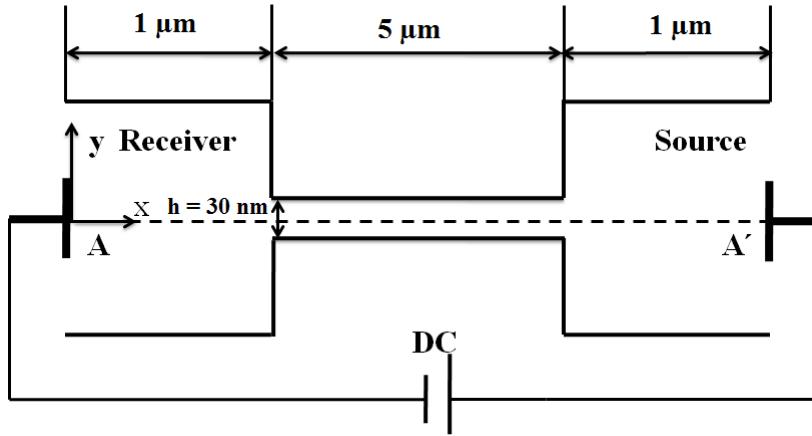

Figure 3.1: Simulation set$-$up (not drawn to scale) equivalent to Daiguji et al. [28] for code validation.

3.3.2 Boundary conditions

The boundary conditions at the walls of the nanochannel are:

$$\mathbf{n}_w \cdot \nabla \phi = \frac{\sigma_{ch}}{\epsilon_0 \epsilon_r}, \quad \mathbf{n}_w \cdot \mathbf{\Gamma}_i = 0 \tag{3.2}$$

where $\mathbf{n}_w$ denotes the unit normal vector (pointing outwards) to the nanochannel surface. On the walls of the nanochannel, the normal flux of each ion is assumed to be zero [41]. A fixed surface charge density, $\sigma_{ch} = -1 \ mC/m^2$ is applied on the nanochannel walls, while the charges on the microchannel walls are considered to be zero as specified by Daiguji et al. [28]. A uniform ionic concentration is assumed to be maintained on the microchannel walls. Thus, the boundary conditions at the walls of the microchannels/reservoirs are given by,

$$\mathbf{n} \cdot \nabla\phi = 0, \quad c_i = c_0 \tag{3.3}$$

where $\mathbf{n}$ here denotes the unit normal vector (pointing outwards) to the reservoir boundary surface and $c_0 = 0.1 \ mM$ is the bulk concentration of the ionic solution. Finally, the boundary conditions at the ends of the source (Equation (3.4)) and receiver (Equation (3.5)) reservoirs are specified as:

$$\phi = \phi^{DC}, \quad c_i = c_0 \tag{3.4}$$

$$\phi = 0, \quad c_i = c_o \tag{3.5}$$

where ϕ^{DC} is the applied DC voltage.

3.3.3 Results

For a charged nanochannel system, the concentration of counterions is higher than the coions due to thick electrical double layers as discussed in chapter 1. The difference in the concentration between the two ions inside the nanochannel is determined by the surface charge density so as to satisfy the electrical neutrality condition. The condition for electrical

neutrality is given by,

$$\frac{1}{h}\int \left(c^+ - c^-\right)\,dy = -\frac{2\sigma_{ch}}{Fh} \tag{3.6}$$

where c^+ and c^- denote the concentration of cation and anion. As the nanochannel walls are negatively charged (with surface surface charge density, $\sigma_{ch} = -1\,mC/m^2$), the concentration of cation is higher than the anion. Fig. 3.2 displays the ionic concentration distribution
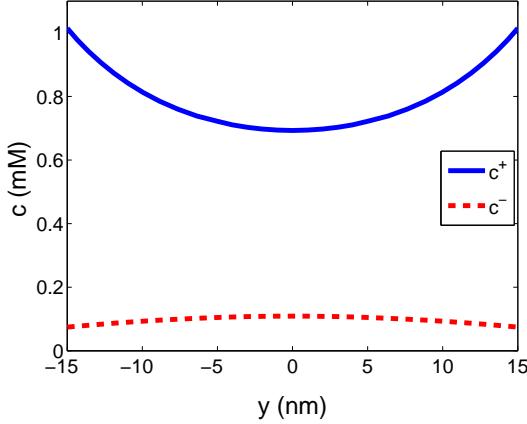

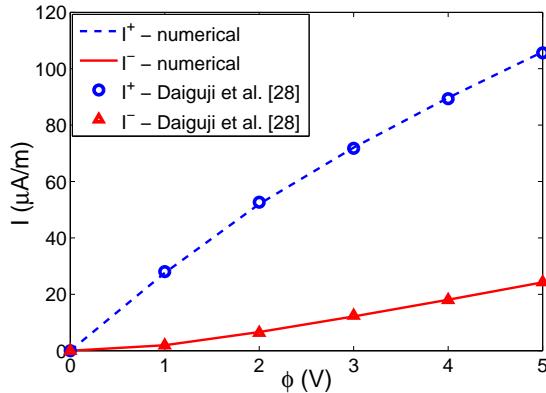Figure 3.2: Numerical results of ionic concentration distribution across the nanochannel at $x = 3500\,nm$.

Figure 3.3: Comparison between numerical and literature [28] results of current−voltage characteristics measured at $x = 3500\,nm$. Note: The data was digitized from the literature plots.

across the nanochannel. From our numerical results, the difference in the ionic concentration averaged across the nanochannel is $0.6918\,mM$, while the average concentration difference

using Equation (3.2) is $0.6910\,mM$. The numerical results are in excellent agreement with the neutrality condition with only $0.1\,\%$ error. Fig. 3.3 shows the comparison between the numerical results of the current$-$voltage characteristics inside the charged nanochannel with the published results of Daiguji et al [28]. Again, the numerical results are in good agreement with the literature results indicating that the solver is accurately able to capture the physics inside the confined systems. The individual ionic currents are calculated using Equation (2.3). Furthermore, the algorithm was also verified with the results published in [29, 30].

Chapter 4

Nonlinear DC electrokinetic flows

In this chapter, we focus our study on the effect of large steady DC electric fields on the electrokinetic transport in micro/nanofluidic interface systems. We discuss the complex physics observed at the interfaces of these devices and also highlight similar findings observed in the literature.

4.1 Simulation model and Boundary conditions

We considered a rectangular nanochannel of 2 μm length (L_0) and 30 nm height (h) connected to two reservoirs (1 μm × 1 μm cross$-$section) on either side of the channel as shown in Fig. 4.1. A $2 - D$ simulation study was carried out by assuming that the depth (perpendicular to the plane of the paper) of the micro and nanochannels to be much larger than the length. Reservoir 1 (on the right side), considered as the source, is given a positive voltage (ϕ^{DC}) and reservoir 2, considered as the receiver (on the left), is grounded. Both the reservoirs are filled with 1.0 mM of KCl buffer solution. We assume that the concentration of H^+ and OH^- is much lower compared to the bulk concentration of the ionic species and hence, the water dissociation effects are not considered in the numerical model [30]. We also neglect the Faradaic reactions that occur near the electrode in the present study. The simulation parameters and the boundary conditions are specified as follows. The operating temperature is $T = 300\ K$, the density and the viscosity of the fluid are 1000 kg/m^3 and $1.003 \times 10^{-3}\ Pa \cdot s$, respectively. The diffusivities of K^+ and Cl^- are $1.96 \times 10^{-9}\ m^2/s$ and $2.03 \times 10^{-9}\ m^2/s$, respectively. A fixed surface charge density, $\sigma_{ch} = -1\ mC/m^2$ is assumed on the walls of the nanochannel [28]. As all the necessary boundary conditions are explained
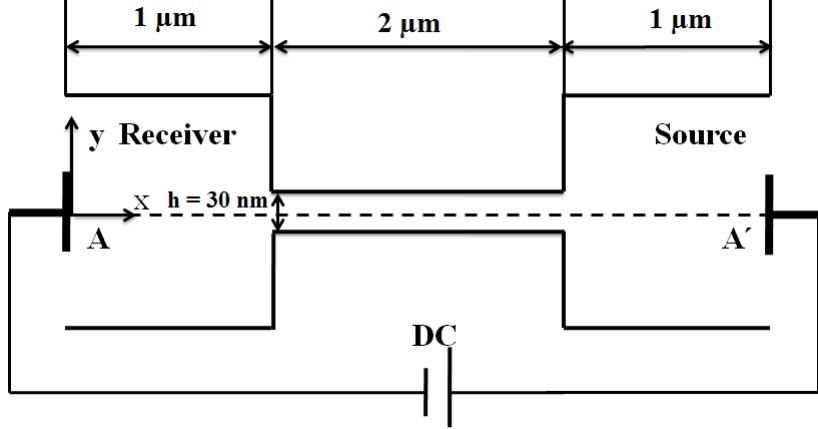
Figure 4.1: Simulation set−up (not drawn to scale), consisting of a nanochannel of height (30 nm) connected to two reservoirs of 1 μm × 1 μm cross−section.

in detail in chapter 2, we briefly describe the same here. The boundary conditions at the walls of the nanochannel are:

$$\mathbf{n}_w \cdot \nabla \phi = \frac{\sigma_{ch}}{\epsilon_0 \epsilon_r}, \quad \mathbf{n}_w \cdot \mathbf{\Gamma}_i = 0, \quad \mathbf{u} = 0, \quad \mathbf{n}_w \cdot \nabla p = 0 \tag{4.1}$$

where $\mathbf{n}_w$ as discussed in the previous chapter denotes the unit normal vector (pointing outwards) to the nanochannel surface. The fluid velocities on both the micro and nanochannel walls are assumed to be subjected to non−slip boundary conditions and the normal flux of each ion is assumed to be zero [41]. Several studies in the recent past [28, 29, 46] have discussed that the nanochannel wall surface charge influences the ion−selectivity of the channel and plays a predominant role on the electrokinetic transport. In all these numerical studies, the charges on the reservoir side walls are assumed to be zero. A similar assumption is made in the present study and the boundary conditions at the walls of the reservoirs are given by,

$$\mathbf{n} \cdot \nabla \phi = 0, \quad \mathbf{n} \cdot \mathbf{\Gamma}_i = 0, \quad \mathbf{u} = 0, \quad \mathbf{n} \cdot \nabla p = 0 \tag{4.2}$$

where $\mathbf{n}$ here denotes the unit normal vector (pointing outwards) to the reservoir boundary surface. Finally, the boundary conditions at the ends of the source (Equation (4.3)) and

receiver (Equation (4.4)) reservoirs are specified as:

$$\phi = \phi^{DC}, \quad c_i = c_0, \quad \mathbf{n} \cdot \nabla \mathbf{u} = 0, \quad p = 0 \tag{4.3}$$

$$\phi = 0, \quad c_i = c_0, \quad \mathbf{n} \cdot \nabla \mathbf{u} = 0, \quad p = 0 \tag{4.4}$$

where c_o is the bulk concentration of the ionic solution. The algorithm to solve the coupled system of PNP and Navier−Stokes equations is displayed in Fig. 4.2. As discussed in chapter 3, an iterative process is implemented within each time loop. A finer mesh is introduced near the walls, at the entrance and exit of the nanochannel. The results discussed here are ensured to be independent of the grid size.
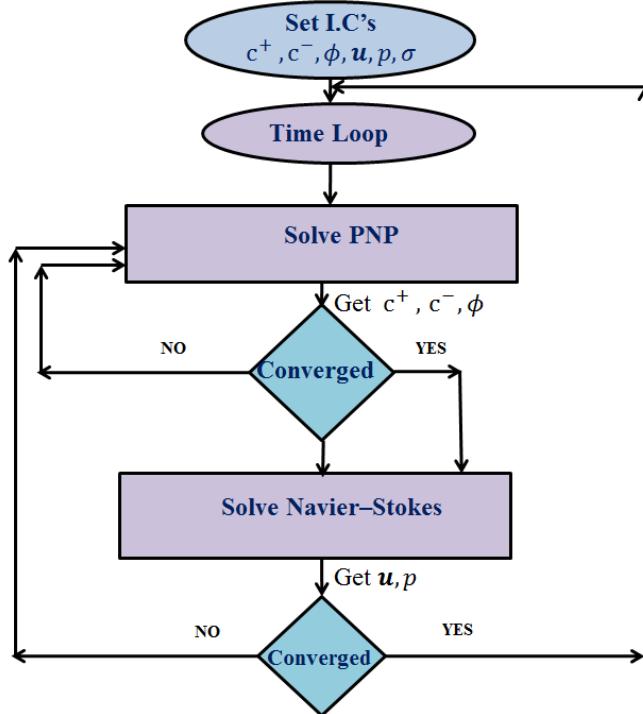

Figure 4.2: Algorithm to solve the coupled transient PNP and Navier−Stokes equations.

4.2 Results and Discussion

4.2.1 Concentration Polarization

Concentration polarization (CP) is a complex phenomenon observed on the integration of micro/nanofluidic devices due to the formation of significant concentration gradients in the electrolyte solution near the interfaces causing accumulation of ions on the cathodic side and depletion of ions on the anodic side for a negatively charged nanochannel surface [47, 48, 49]. The accumulation and depletion physics observed near the interfaces is summarized below. For a negatively charged nanochannel, the EDL would be positively charged. For a thick
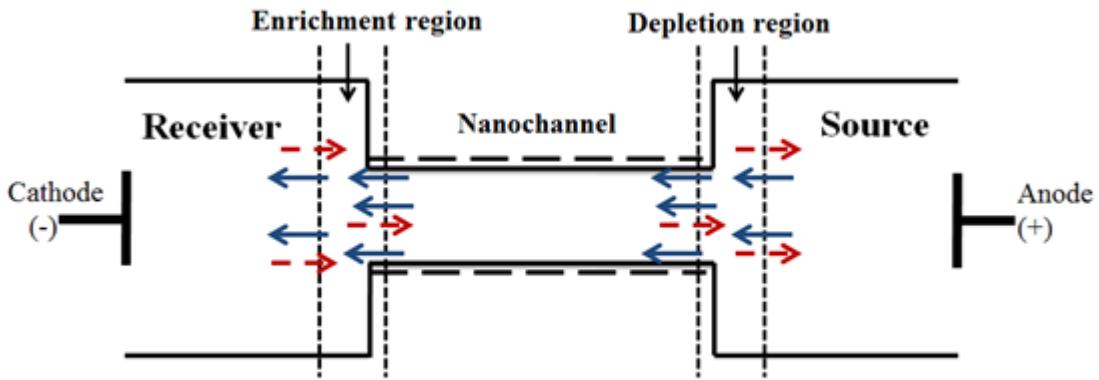

Figure 4.3: Schematic illustration of ion−enrichment and ion−depletion effect in cation−selective micro/nanofluidic channel. The solid arrows indicate the flux of cations and the dotted arrow indicate the flux of anions. At the nanochannel−anodic junction, both the anions and cations are depleted, while there is an enhancement of both the ions at the cathode−nanochannel junction.

EDL, as discussed in chapter 1, the nanochannel becomes ion−selective, resulting in higher cation concentration than anions. Thus, the flux of cations is higher compared to the anions in the nanochannel. With the application of positive potential at the source microchannel (reservoir), the cations move from the source (anode) reservoir to the receiving (cathode) reservoir end, while the anions move in the opposite direction through the nanochannel. At the cathodic side, the anion flux from the ends of reservoir to the nanochannel junction is

higher compared to the anion flux from the junctions to the nanochannel as the anions are repelled by the negatively charged nanochannel. This difference in fluxes causes an accumulation of anions at the cathode−nanochannel junction. The cation flux from the nanochannel to the cathode junction is greater than from the cathode junction to the reservoir as the cations have to balance the anions present at this junction. This results in an accumulation of cations as well at the nanochannel−cathode junction. At the anodic side, the anion flux from the nanochannel to the anode junction can't balance the anion flux from the anode junction to the reservoirs due to the limited anions passing through the nanochannel. This results in a depletion of anions at this junction. The cation flux from the reservoir to the anode−nanochannel junction is less than the cation flux entering the nanochannel as the cations are attracted by the positively charged nanochannel. This in turn leads to the depletion of cations at this junction. The phenomenon is reversed for a positively charged nanochannel surface. Fig. 4.3 shows a schematic diagram highlighting the accumulation and
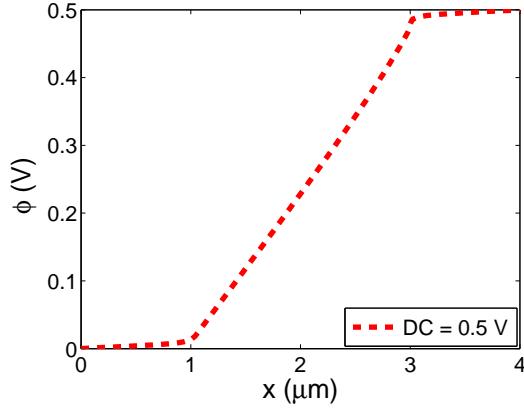

Figure 4.4: Axial potential distribution for a low DC electric field (DC = 0.5 , V). The voltage drop is linear along the entire nanochannel.

the depletion physics. This phenomenon was also extensively studied in the field of colloid science and in membrane science for over 40 years and the early works of CP phenomenon is comprehensively reviewed by Rubinstein et al. [50]. Further, such complex phenomenon couldn't be postulated using the classical equilibrium model of EDL [50]. It is important to note that for low DC voltages (DC = 0.5 V), the electrical potential drop mainly occurs
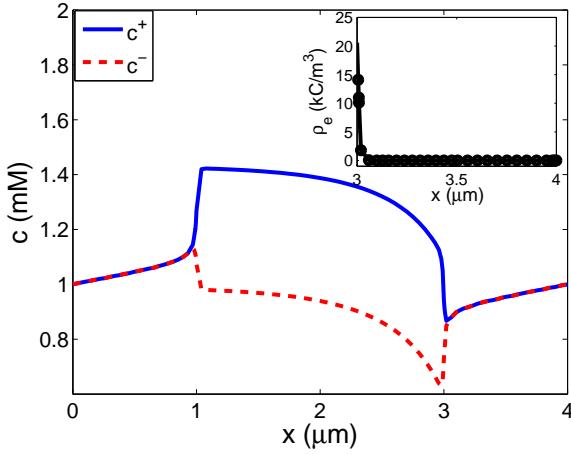
Figure 4.5: Axial ionic concentration distribution for a low DC electric field (DC = $0.5\,V$). Linear concentration gradient with local electroneutrality maintained at both the interfaces. The inset of the figure indicates no space charge variation at the anodic interface.

inside the nanochannel as the resistance in the nanochannel is much larger than that in the reservoirs. The potential drop at such voltages can be assumed to be linear inside the nanochannel (see Fig. 4.4). We observe a linear concentration gradient at both the cathode (enrichment) and anode (depletion) interfaces as shown in Fig. 4.5. At this voltage, we observe local electroneutrality of ions at both the interfaces with no space charge at these interfaces. Also, there is no variation of the electroosmotic flow near the interfaces. However, at large DC voltages, several interesting features are observed at the interfaces of the micro/nanofluidic systems which is discussed in the next section.

4.2.2   Induced space charge and Nonlinear electroosmosis

On application of large electric fields (DC = $5.0\,V$), many interesting physics is observed especially at the depletion interface regions. We no longer observe a linear concentration gradient near the depletion interface (i.e, at the anodic interface in the present study). Fig. 4.6 shows the axial concentration distribution in these devices for large electric fields. It is observed that the electroneutrality is maintained at the enrichment (cathodic) interface while there is a region of induced space charge near the depletion interface. The electrical
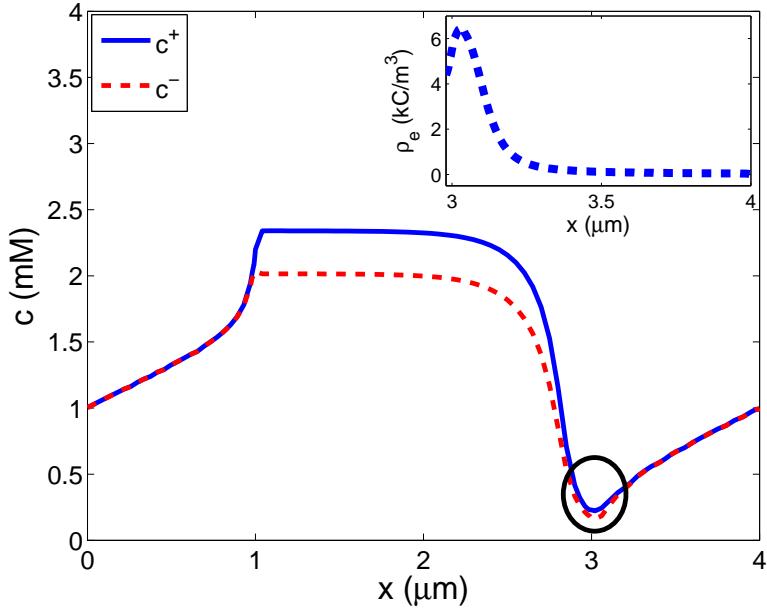
Figure 4.6: Axial ionic concentration distribution for a large DC electric field (DC $= 5\,V$). Linear concentration gradient with local electroneutrality being maintained at the enrichment interface, while there is an induced space charge observed at the depletion (anodic) interface. The inset of the figure indicates the induced space charge variation at the anodic depletion interface for large DC electric fields.

resistance at the enrichment region is very small while the low ionic concentrations at the depletion interface and the presence of induced space charges lead to a large resistance at this region which in turn results in a large potential drop [51] as shown in Fig. 4.7. Hence, the potential distribution inside the nanochannel is no longer linear for large DC voltages. Further, it is observed that the induced space charges under the action of the external electric field leads to nonlinear electroosmosis with the generation of electrokinetic vortices at these interfaces along with inducing large pressure gradients at this junction as shown in Fig 4.8 and Fig. 4.9 respectively. Thus, the flow is no longer irrotational under large DC electric fields. Another interesting observation is that the vortices developed at these interface regions rotate in opposite directions.

Experiments performed by Kim et al., [52] and Yossifon et al., [53] also reveal the non-equilibrium EOF near the micro/nanofluidic junctions. The application of electric field on the surface of particles also results in such induced space charges which spread over a larger
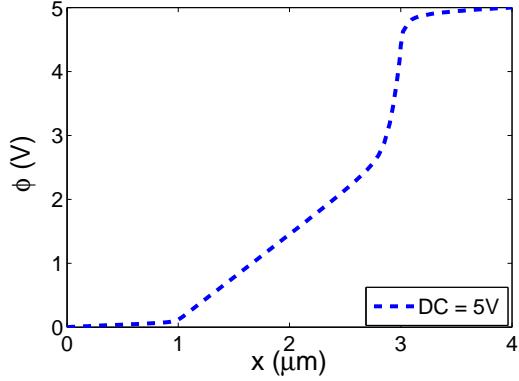
Figure 4.7: Axial nonlinear potential distribution for a large DC electric field (DC = $5.0\,V$).

| (a) | (b) |
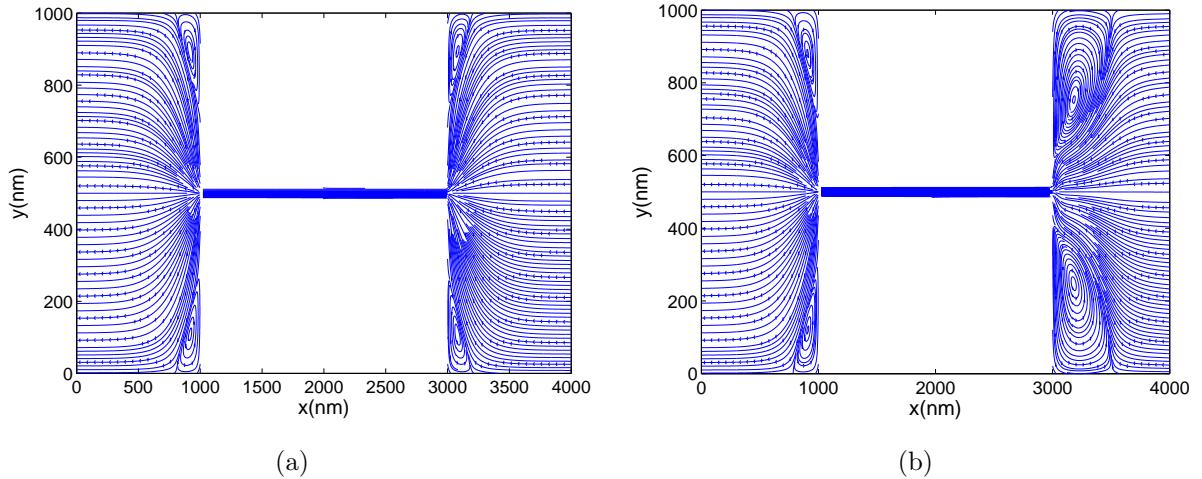
Figure 4.8: Streamline plots of electrokinetic velocity for (a) low DC electric fields (DC = $0.5\,V$) and (b) large DC electric fields (DC = $5.0\,V$). The induced space charges at the depletion interface leads to the generation of vortices at these interfaces.

region than the primary EDL resulting in highly chaotic flow patterns. A recent review by Höltzel and Tallarek [54] provide a detailed discussion on the polarization effects around membranes, packed beds and glass monoliths.

With the understanding of nonlinear electrokinetic flow characteristics under large DC fields, we investigate the electrokinetic transport under combined AC and DC fields in micro/nanofluidic interconnect devices in our next chapter.

Figure 4.9: Axial nonlinear pressure distribution for a large DC electric field (DC = 5.0 V). The induced space charge results in large induced pressure gradients near the depletion interface.
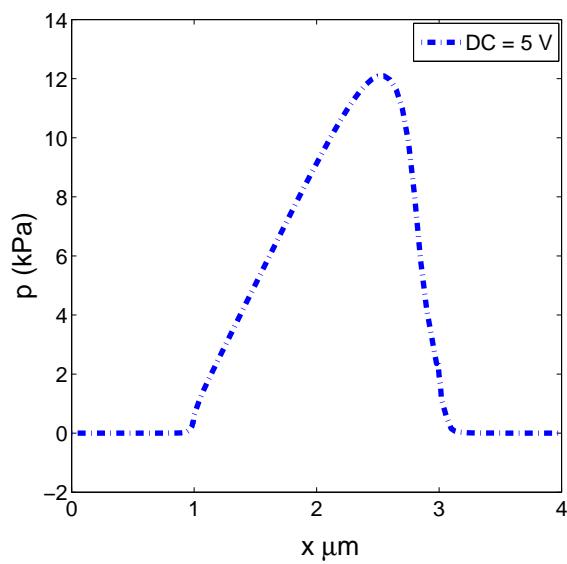
Chapter 5

Nonlinear AC/DC electrokinetic transport

5.1 Introduction

AC electroosmosis has emerged as a predominant technique in driving the fluids in DNA hybridization [55], enhance species mixing in microfluidic devices [56, 57], etc. Ajdari [58] has theoretically predicted uni−directional fluid flow on application of AC electric fields using asymmetric microelectrodes placed on the surface of the microchannel. This was later experimentally observed by Brown et al. [59]. Ramos et al. [60] theoretically analyzed the pumping phenomena using an electroosmotic model. Dutta et al. [61] and Erickson and Li [62] presented analytical solutions for AC electroosmotic flows in a 2−D straight microchannel. AC electroosmotic flow in curved microchannels was numerically investigated by Chen et al. [63] and showed that the strength of the secondary vortices decreases with increase in the frequency. Olesen et al. [64] analyzed the nonlinear response of the electrolyte solution under large AC voltages using a simple parallel plate blocking electrode model. Although significant progress has been made in understanding AC effects in microfluidic devices, few reports are available with regard to the combined effect of AC and DC fields on the nanoscale systems [65]. An extensive numerical study based on the continuum theory is carried out to understand the electrokinetic transport and other hydrodynamic effects under the application of combined AC and DC electric fields in micro/nanofluidic interface devices. The results are elaborately discussed in this chapter. The simulations are carried out for different EDL thickness and nanochannel wall surface charge density to study the flow characteristics. We observe many anomalous and counter−intuitive phenomena under thick EDL regime and at high nanochannel wall surface charge density (in other words, when

the nanochannel is highly ion−selective), as the net fluid flow changes from those obtained on the application of only a DC source. These effects are predominantly due to the nonlinear potential distribution along with the presence of dual concentration polarization space charges observed near both the interfaces of micro/nanochannel at amplitudes greater than the DC voltage and at low Strouhal number. The large temporal and spatial variations in the polarization space charges near the interfaces lead to finite inertia effects resulting in anomalous changes to the electroosmotic velocity. We calculate the time averaged electroosmotic velocity from the temporal numerical solution and understand its deviation from the DC electroosmotic velocity. We believe that these studies would provide a better understanding on the electrokinetic transport in improving the design of new micro/nanofluidic interface devices for sample stacking, mixing, reaction kinetics and species separation. The coupled PNP and Navier−Stokes equations discussed elaborately in chapter 2 are used to understand the transport phenomenon under combine AC and DC fields.

5.2   Simulation model and Boundary conditions

We considered a similar geometry as discussed in chapter 4 for our present analysis (see Fig. 5.1). A $2 - D$ simulation study was carried out by assuming that the depth (perpendicular to the plane of the paper) of the micro and nanochannels to be much larger than the length. Reservoir 1 (on the right side), considered as the source, is given a positive voltage (ϕ^{DC}) and reservoir 2, considered as the receiver (on the left), is grounded. An AC voltage is applied after the system reaches a steady state with the DC field. Similar boundary conditions as discussed in chapter 4 is applied here. The only variation is the boundary condition for the potential at the source reservoir (see Equation (5.1)).
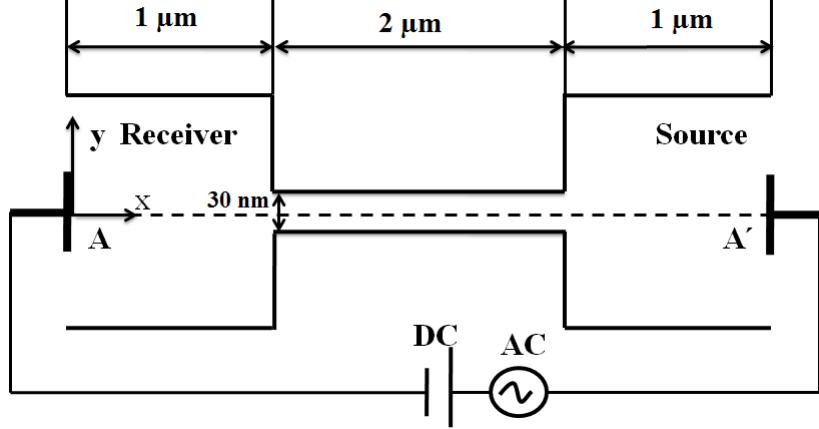
$$\phi = \phi^{DC} + \phi^{AC} sin(\omega t) \tag{5.1}$$

Figure 5.1: Simulation set−up (not drawn to scale), consisting of a nanochannel of height (30 nm) connected to two reservoirs of 1 μm × 1 μm cross−section. AC potential is applied after the initial transients under the DC field die out.

where ϕ^{DC} is the applied DC voltage, ϕ^{AC} is the amplitude of the AC electric potential and ω is the angular frequency ($\omega = 2\pi f$, f is the applied frequency).

We nondimensionalize all the equations by scaling the distance with the length of the nanochannel (L_0), time with the frequency time scale ($1/f$), concentration with the bulk concentration of the electrolyte solution (c_0), electric potential with $\phi_0 = RT/Fz$, fluid velocity with $U_0 = \epsilon_0 \epsilon_r E_0 \phi_0 / \mu$, where E_0 is the average applied field in the nanochannel (i.e., it is the total voltage drop divided by the nanochannel length), pressure with $p_0 = \mu U_0 / L_0$, and space charge density with $\rho_{e_0} = Fzc_0$. Further, we consider a symmetric monovalent electrolyte ($z_+ = -z_- = z$) like KCl in the present analysis. We normalize the diffusion coefficient of each ionic species with the characteristic diffusion coefficient ($D_0 = 2 \times 10^{-9}\, m^2/s$). Applying these scaling variables, the system of governing equations in the dimensionless form can be written as:

Conservation of mass

$$\nabla^* \cdot \mathbf{u}^* = 0 \tag{5.2}$$

32

Conservation of momentum

$$\left(St\frac{\partial \mathbf{u}^*}{\partial t^*} + \mathbf{u}^* \cdot \nabla^* \mathbf{u}^* \right) = \frac{1}{Re}\left(-\nabla^* p^* + \nabla^{*2}\mathbf{u}^* + \frac{1}{2\beta^2}\rho_e^* \mathbf{E}^* \right) \tag{5.3}$$

Transport of positive ions,

$$\left(St\frac{\partial c_+^*}{\partial t^*} + \nabla^* \cdot (c_+^* \mathbf{u}^*) \right) = \frac{1}{Pe}\left(D_+^* \nabla^{*2} c_+^* + D_+^* \nabla^* \cdot (c_+^* \nabla^* \phi^*) \right) \tag{5.4}$$

Transport of negative ions,

$$\left(St\frac{\partial c_-^*}{\partial t^*} + \nabla^* \cdot (c_-^* \mathbf{u}^*) \right) = \frac{1}{Pe}\left(D_-^* \nabla^{*2} c_-^* - D_-^* \nabla^* \cdot (c_-^* \nabla^* \phi^*) \right) \tag{5.5}$$

Poisson equation for electrical potential,

$$\nabla^{*2}\phi^* = -\frac{1}{2\beta^2}\rho_e^* \tag{5.6}$$

In the above equations, variables with superscript $'*'$ are the dimensionless variables. The various nondimensional numbers are given by, $\beta = \lambda_D/L_0$, Peclet number, $Pe = L_0 U_0/D_0$, Reynolds number, $Re = \rho U_0 L_0/\mu$, and Strouhal number, $St = fL_0/U_0$. The Debye length (λ_D), determining the thickness of the EDL, is defined as, $\lambda_D = \sqrt{\epsilon_0 \epsilon_r RT/2F^2 z^2 c_0}$. The inherent time scales present in the system are the viscous time scale (L_0^2/ν) (where $\nu = \mu/\rho$, is the kinematic viscosity of the fluid), convective time scale (L_0/U_0) and the molecular diffusion time scale (L_0^2/D_0). In the present study, we are interested in understanding the AC effects on the electroosmotic fluid velocity for different EDL thickness, hence, the important nondimensional numbers investigated are the Strouhal number (St) and the nondimensional Debye length (β). The results reported here are again ensured to be independent of the grid size.

5.3 Results and Discussion

We initially consider low bulk ionic concentration, $c_0 = 1\,mM$ (corresponding to a thick EDL regime, $\beta = 0.0049$) and a nanochannel wall surface charge density, $\sigma_{ch} = -1\,mC/m^2$ (corresponding to a normalized nanochannel wall surface charge density, $\sigma^* = \sigma_{ch}L_0/\epsilon_0\epsilon_r\phi_0 = -109.227$) to investigate the effect of combined AC/DC electric fields on the electrokinetic transport. At this low ionic concentration, the nanochannel is found to behave as an ion–selective membrane leading to the predominant transport of counterions inside the nanochannel. Under these thick EDL limits, we discuss the anomalous electroosmotic transport physics observed inside the nanochannel under different AC/DC electric fields. In order to understand the anomalies and the nonlinear effects in the electrokinetic transport, we calculate the time averaged potential, body force, pressure, velocity and compare them with the DC case. We note that for a nonlinear system, depending on the degree of nonlinearity, the time averaged quantities under AC/DC electric field need not be equal to the DC value. Several numerical and experimental studies in the recent past have observed the ion–selectivity of the nanochannel to depend on both the bulk ionic concentration and the nanochannel wall surface charge density [11, 48, 49]. We extend our study to discuss the influence of combined AC/DC electric fields on the electrokinetic transport for different dimensionless EDL thickness and nanochannel wall surface charge density.

5.3.1 Nonlinear potential distribution

As discussed earlier, the integration of micro/nanofluidic devices leads to many complex phenomena [11, 30, 66]. The most important phenomenon among them is concentration polarization, [48, 52, 67] (CP) which is predominantly observed in highly ion–selective nanochannel on the application of large DC voltages [53] due to the formation of significant concentration gradients in the electrolyte solution near the interfaces causing accumulation of ions on the cathodic side and depletion of ions on the anodic side for a negatively

charged nanochannel surface. At low DC voltages, the electrical potential drop mainly occurs inside the nanochannel as the resistance in the nanochannel is much larger than that in the reservoirs. The potential drop at such voltages can be assumed to be linear inside the nanochannel. However, at large DC voltages the resistance is very small on the cathodic enrichment side, while the low ionic concentration and the presence of induced polarization space charges at the anodic depletion interface region leads to a large resistance at this region which in turn results in a large potential drop near the anodic junction as shown in the inset of Fig. 5.2(a). Thus, under large DC electric fields interesting polarization physics is observed near the anodic interface region of micro/nanochannel and the presence of induced polarization space charges can be understood from the large potential drop developed at this interface region. The polarization effects observed under DC electric fields in ion−selective nanochannels have been extensively studied in the literature [30, 51].

We focus our attention to investigate the effect of combined AC and DC electric fields on the electric potential distribution. We note that in the present study, for a typical DC voltage of about $0.5\,V$ and a characteristic length scale of about $2\,\mu m$, the characteristic velocity is about $4.6\,mm/s$. For such a system, the convective time scale is approximately $0.44\,ms$. Further, the kinematic viscosity (ν) of water at $300\,K$ is around $1.003 \times 10^{-6}\,m^2/s$, resulting in an approximate viscous time scale of $4\,\mu s$. These time scales are relevant as we investigate AC electric fields with different frequencies, ranging from $500\,Hz - 1\,MHz$ to consider different Strouhal number, St. AC voltages of different amplitudes (ranging from $0.1\,V - 10\,V$) are considered to understand the effect of the ratio, $\alpha = \phi^{AC}/\phi^{DC}$, on the nonlinear potential distribution. As expected, under small AC amplitude ($\alpha = 0.2$), there is no change in the system behavior and the response of the time averaged axial potential distribution is similar to the DC case as shown in Fig. 5.2(a). Furthermore, similar physics is observed at all St. The time averaged potential at each position along the centerline of

the channel is calculated as:

$$\langle \phi^*(x^*) \rangle = \frac{1}{T} \int_0^T \phi^*(x^*) \, dt \tag{5.7}$$

It can be shown that, for small α (at any St), the time averaged axial electroosmotic velocity due to the combined AC+DC electric field can be obtained using the principle of linear superposition,

$$\langle u^*_{AC+DC} \rangle = u^*_{DC} + \langle u^*_{AC} \rangle \tag{5.8}$$

where $\langle \rangle = \frac{1}{T} \int_0^T () \, dt$, is the time averaged component and T is the time period of one cycle. The time averaged velocity of the AC component is zero, hence, as expected the electrokinetic flow is unaffected under small AC perturbations. However, similar to the nonlinear potential distribution observed in micro/nanofluidic channels under a large DC voltage, the application of combined AC/DC electric fields at amplitudes greater than the DC field (i.e., $\alpha > 1$) and at low St also introduces several changes to the potential distribution, leading to many counter−intuitive and anomalous effects in the electrokinetic transport. It is observed that, during the first half of the cycle, the combined high amplitude AC along with a relatively low DC voltage causes a large voltage drop (as DC acts in the same direction as the AC voltage) near the anodic interface and no significant voltage drop is observed near the cathodic interface. However, during the other half of the cycle, the combined AC+DC voltage causes a voltage drop near the cathodic interface and no significant voltage drop is observed near the anodic interface. It is important to note that the voltage drop observed near the cathodic interface in this half cycle is relatively smaller (as DC acts against the AC voltage) compared to the voltage drop observed near the anodic interface during the first half of the cycle. Hence, the application of large AC amplitude at low St along with a relatively low DC voltage results in a large voltage drop near the anodic interface and a relatively smaller drop of potential near the cathodic interface. Fig. 5.2(a) and Fig. 5.2(b) show the time averaged nondimensional axial electrical potential distribution for different

α and St, respectively. We discuss the frequency effects in detail in the later part of this section.
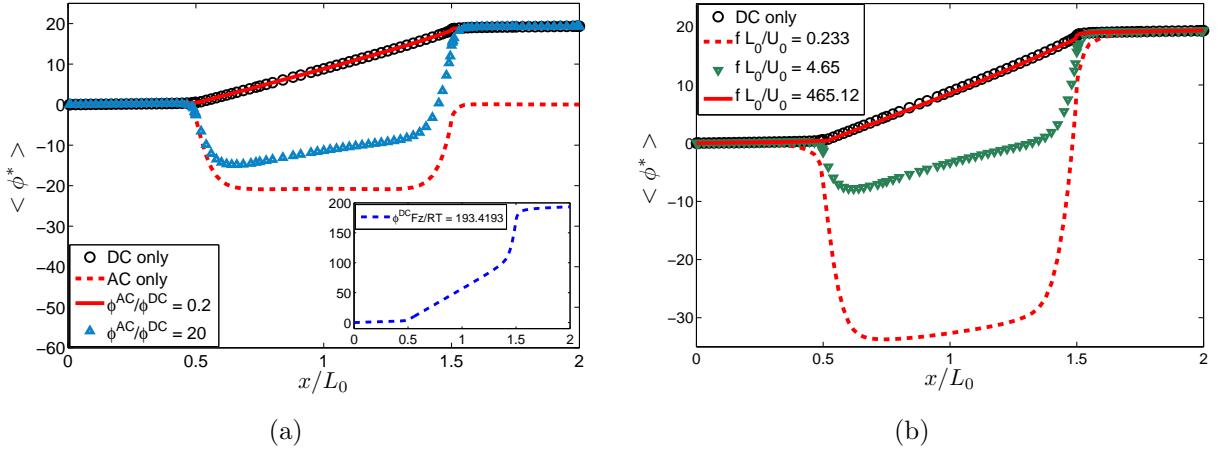

(a)

(b)

Figure 5.2: (a) Numerical results of time averaged nondimensional axial potential distribution for different α ($= \phi^{AC}/\phi^{DC}$) at a fixed $St = 4.65$. Note: For the AC only case, $\phi^{AC} Fz/RT = 386.84$ and $St = 4.65$. The inset of the figure shows nondimensional axial potential distribution for a large DC voltage, $\phi^{DC} Fz/RT = 193.419$. At this voltage, there is a large voltage drop observed at the anodic junction of micro/nanochannel due to the concentration polarization space charges induced at this junction (b) Variation of time averaged nondimensional axial potential distribution for different St ($= fL_0/U_0$) at a fixed $\alpha = 16$. In all these cases the applied DC voltage $\phi^{DC} Fz/RT = 19.3419$, $\beta = 0.0049$ and $\sigma^* = -109.227$.

The regions (with significant voltage drops as shown in Fig. 5.2(a) and Fig. 5.2(b)) near both the interfaces are identified as the concentration polarization space charge regions and the lengths of these polarization charge regions are determined by measuring the large voltage drop regions as shown schematically in Fig. 5.3. Thus, we observe dual concentration polarization regions (region I, denoted as CPL−I near the anodic interface and region II, denoted as CPL−II near the cathodic interface) unlike the DC only case where the large voltage drop (for a negatively charged nanochannel) occurs predominantly at the anodic junction due to the polarization space charge regions developed at this junction. Further, the dual polarization lengths are not equal to each other (CPL−I > CPL−II) due to the unequal voltage drops at both the interfaces. We would also like to point out that the large potential drop occurs from the inner regions of the nanochannel junction and propagate towards the

37

microchannel/reservoir junction as shown in Fig. 5.2(a) and Fig. 5.2(b). Thus, the sum of the lengths inside the nanochannel junction and the reservoir junction together constitute the total CPL length. Similar phenomenon of polarization space charge propagation from the inner regions of the nanochannel anodic junction towards the reservoir are observed in the experimental and numerical studies of Mani et al. [48, 49] under DC electric fields.
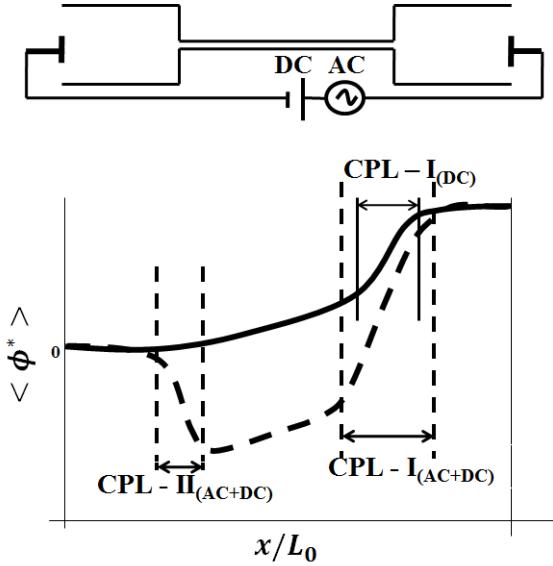

Figure 5.3: Schematic of the potential distribution along the length of the micro/nanochannel. The regions with large voltage drops near both the micro/nanofluidic interfaces are defined as concentration polarization regions. CPL−I represents the polarization length at the right end (anodic end) of the nanochannel, while CPL−II indicates the polarization length at the cathodic end. The subscripts DC and AC+DC indicate the lengths when the corresponding fields are applied (the solid line and the dashed line indicate the approximate potential profile for large DC voltage, and large α (and low St) AC+DC field, respectively).

Fig 5.4(a) shows the normalized CPL as a function of α, at a constant frequency ($St = 4.65$) and DC voltage ($\phi^{DC} F z / RT = 19.3419$). We discuss two key observations from the figure. First, dual concentration polarization space charge regions are developed at both the interface regions of micro/nanochannel when the amplitude of the AC field is greater than the DC field ($\alpha > 1$). Second, it is observed that the polarization lengths developed at both the interface regions increase monotonically with α. It is important to note that along with the amplitude, the frequency of the AC field also plays an important role in

controlling the polarization space charges at the interfaces. Fig. 5.2(b) shows the time averaged nondimensional axial potential distribution for different St at a constant amplitude ($\alpha = 16$) and DC voltage ($\phi^{DC} Fz/RT = 19.3419$). It can be observed that for low St ($St = 0.233$ and $St = 4.65$) large voltage gradients and dual concentration polarization charge regions are developed at both the interface regions of micro/nanochannel. However, at large St ($St = 465.12$) or when the frequency time scale is comparable to the viscous time scale (L_0^2/ν), the AC polarization and nonlinear effects decrease and the potential distribution follows the DC case. Fig 5.4(b) displays the normalized CPL as a function of St to further illustrate the aforementioned physics. Thus, under thick EDL regime, the dual concentration polarization space charge regions (with unequal lengths) are developed at both the interface regions of a micro/nanofluidic device under low St and for $\alpha > 1$. The same scaling physics is observed even for the case of a higher DC voltage, displayed in the inset of Fig. 5.4(a) where the dual polarization charge regions are built up as $\alpha > 1$. By controlling these polarization lengths we can control the nonlinear effects inside the nanochannel.

(a)   (b)
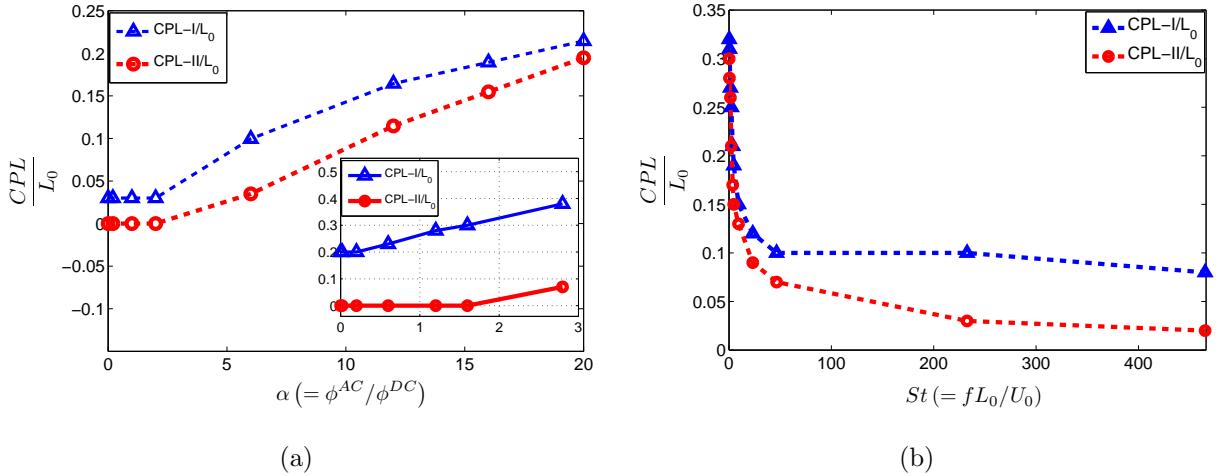
Figure 5.4: Normalized dual concentration polarization lengths measured at a fixed $\beta = 0.0049$, $\sigma^* = -109.227$ (a) as a function of α at a fixed $St = 4.65$ and $\phi^{DC} Fz/RT = 19.3419$. The inset of the figure displays the dual concentration polarization lengths for a large DC voltage, $\phi^{DC} Fz/RT = 193.419$ (b) as a function of St at a fixed $\alpha = 16$ and $\phi^{DC} Fz/RT = 19.3419$. The resolution of the lengths measured is limited by the grid spacing.

5.3.2 AC effects on electrostatic body force and induced pressure

We discuss the effects of nonlinear potential distribution and the dual concentration polarization space charge regions on the electrostatic body force and pressure distribution. Fig. 5.5 shows a comparison of the nondimensional axial body force distribution between a low DC field, $\phi^{DC}Fz/RT = 19.3419$ and a combined AC/DC electric field with $\alpha = 20$, $St = 4.65$ and same DC voltage. For this AC/DC electric field, we observe large body force gradients at both the interface regions of micro/nanochannel compared to the DC case. These observations are primarily due to the large voltage gradients and the polarization space charges observed near both the interface regions as discussed in the previous section. The axial body force ($\mathbf{f}_x$) displayed in Fig. 5.5 is averaged across the nanochannel and is calculated as:

$$\mathbf{f}_x = \frac{1}{h} \int_{\frac{-h}{2}}^{\frac{h}{2}} \rho_e \mathbf{E}_x \, dy \tag{5.9}$$

where the subscript x denotes the $x-$component. The body force is further normalized with the characteristic body force $\rho_{e_0}E_0$.

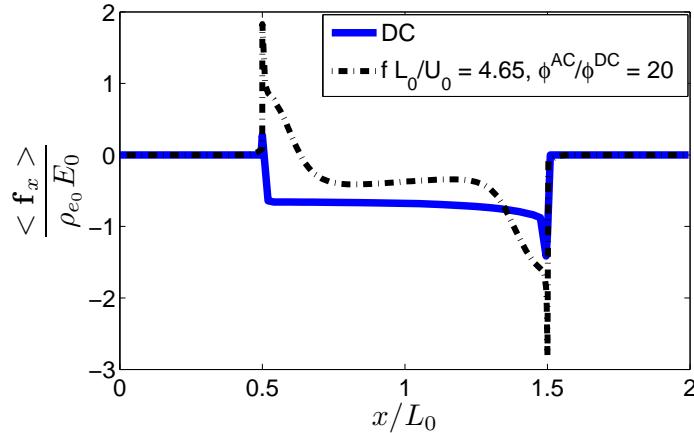Figure 5.5: Nondimensional axial body force distribution (averaged over one time period and averaged across the cross−section) for different electric fields at a fixed $\beta = 0.0049$, $\sigma^* = -109.227$ and $\phi^{DC}Fz/RT = 19.3419$.

Fig. 5.6(a) displays the time averaged nondimensional axial pressure distribution for different α. To understand the amplitude effects, frequency ($St = 4.65$) and DC voltage

($\phi^{DC}Fz/RT = 19.3419$) are kept constant. It can be observed that under small AC perturbations ($\alpha = 0.2$), the time averaged AC/DC axial pressure distribution shows minimal variation compared to that from the DC field, while the application of higher AC amplitudes ($\alpha = 20$) results in large induced pressure gradients at both the interface regions of micro/nanochannel due to the large voltage gradients and electrostatic body force observed at these interface regions. Furthermore, this is unlike the physics observed under large DC voltage (see inset of Fig. 5.6(a)) where large induced pressure gradients are observed only at the anodic interface region. These results further illustrate the presence of dual polarization space charge regions under combined AC/DC electric fields. Fig. 5.6(b) shows the time av-
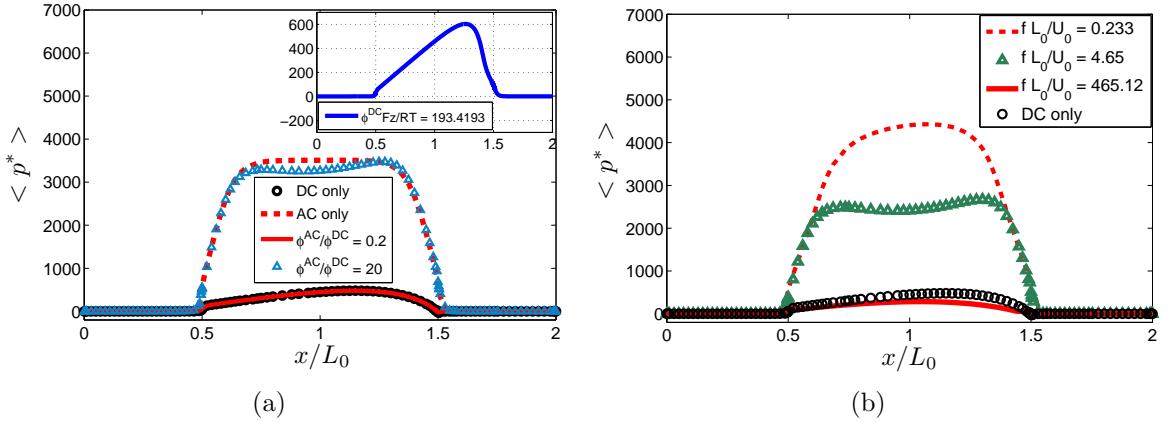

Figure 5.6: (a) Time averaged nondimensional axial pressure distribution for different α at a fixed $St = 4.65$. Note: For the AC only case, $\phi^{AC}Fz/RT = 386.84$ and $St = 4.65$. The inset of the figure shows nondimensional axial pressure distribution for a large DC voltage, $\phi^{DC}Fz/RT = 193.419$. At this voltage, there is a large induced pressure gradient near the anodic junction of micro/nanochannel due to the concentration polarization space charges induced at this junction. (b) Variation of time averaged nondimensional axial pressure distribution for different St at a fixed $\alpha = 16$. In all these cases $\beta = 0.0049$, $\sigma^* = -109.227$ and $\phi^{DC}Fz/RT = 19.3419$.

eraged nondimensional axial pressure distribution for different St. To study the frequency effects, the amplitude ($\alpha = 16$) and DC voltage ($\phi^{DC}Fz/RT = 19.3419$) are kept constant. It can be observed that for low St ($St = 0.233$ and $St = 4.65$) large induced pressure gradients are developed at both the interface regions of micro/nanochannel. However, at large

St ($St = 465.12$) or when the frequency time scale is comparable to the viscous time scale, the nondimensional axial pressure distribution follows the DC case indicating minimal AC dependence. This can be understood from the fact that the AC polarization effects and voltage gradients also follow the same scaling physics with respect to St as discussed in the previous section. In order to understand the effect of voltage gradients and the polarization space charge regions on the electroosmotic velocity inside the nanochannel, we first discuss its effect on the total electrostatic body force acting inside the nanochannel as the electroosmotic velocity is directly dependent on the total electrostatic body force. The total electrostatic body force ($\mathbf{F}_x$) integrated over the entire channel is calculated as:

$$\mathbf{F}_x = \int_{x_s}^{x_s+L_0} h\, \mathbf{f}_x\, dx \tag{5.10}$$

where x_s is the x coordinate where the nanochannel starts, the subscript x denotes the $x-$component and $\mathbf{f}_x$ is the body force averaged across the nanochannel obtained from Equation (5.9).

Figure 5.7: Ratio of the total axial electrostatic body force (averaged over one time period) integrated over the entire channel under combined AC/DC electric field to the total DC axial electrostatic body force for a fixed $\beta = 0.0049$, $\sigma^* = -109.227$ and $\phi^{DC}Fz/RT = 19.3419$, (a) as a function of α at a fixed $St = 4.65$ (b) as a function of St at a fixed $\alpha = 16$.

Fig. 5.7(a) displays the ratio of the total axial electrostatic body force (averaged over

one time period and integrated over the entire channel) under combined AC/DC electric field to the total DC axial electrostatic body force as a function of α at a constant frequency ($St = 4.65$) and DC voltage ($\phi^{DC} Fz/RT = 19.3419$). It is observed that the ratio of the total electrostatic body force acting inside the nanochannel decreases quadratically with respect to α. We understand that the increase in the polarization lengths at the interfaces result in a decrease in the time averaged total AC/DC axial electrost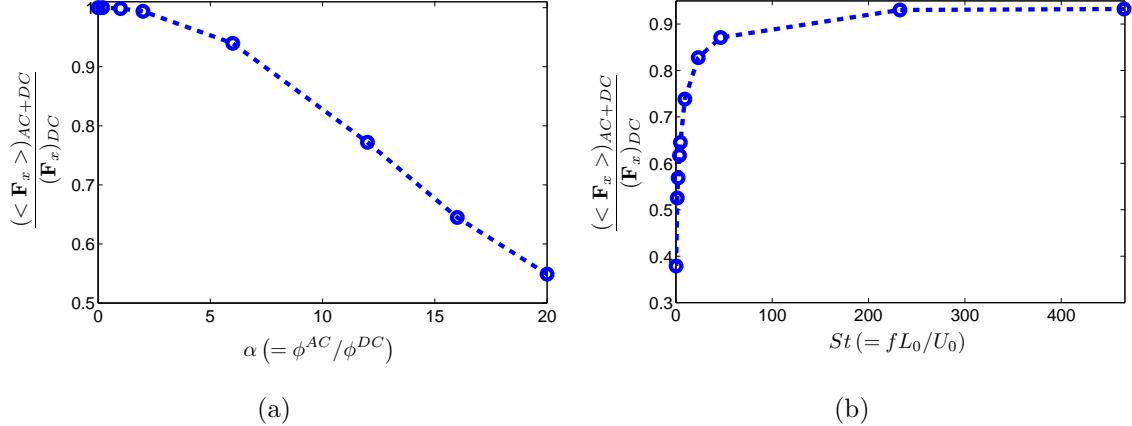atic body force acting inside the nanochannel. Fig. 5.7(b) shows the ratio of the total axial electrostatic body force (averaged over one time period and integrated over the entire channel) under combined AC/DC electric field to the total DC axial electrostatic body force as a function of St. To study the frequency effects, the amplitude ($\alpha = 16$) and DC voltage ($\phi^{DC} Fz/RT = 19.3419$) are kept constant. It can be seen that the time averaged total AC/DC axial electrostatic body force decreases compared to the total DC axial electrostatic body force at low St. However, at large St or when the frequency time scale is comparable to the viscous time scale, the time averaged total AC/DC axial electrostatic body force show minimal variation compared to the total DC axial electrostatic body force. These results again can be understood from the fact that the dual concentration polarization space charges and strong voltage gradients at both the interfaces are observed at low St. However, at large St, the AC polarization effects are minimal as discussed elaborately in the previous section.

5.3.3   Electroosmotic flow

With the understanding of the effect of combined AC/DC electric fields on the total electro-static body force, we investigate the effect of these electric fields on the axial electroosmotic flow (EOF) velocity inside the nanochannel. Fig. 5.8(a) shows the ratio of the time av-eraged AC/DC axial electroosmotic velocity to the DC axial electroosmotic velocity as a function of α. To understand the amplitude effects, frequency ($St = 4.65$) and DC voltage ($\phi^{DC} Fz/RT = 19.3419$) are kept constant and the electroosmotic velocity is evaluated at the midpoint of the nanochannel. It is observed that the ratio of the time averaged AC/DC

axial electroosmotic velocity inside the nanochannel decreases quadratically with respect to α. This can be understood from the fact that the ratio of the time averaged total AC/DC axial electrostatic body force to the total DC axial electrostatic body force exhibits a similar scaling relation with respect to α and the underlying physics is already discussed in the earlier section. The inset of Fig. 5.8(a) also reveals similar scaling physics with respect to α under a higher DC voltage ($\phi^{DC}Fz/RT = 193.419$). The deviation of time averaged AC/DC velocities from the DC velocity illustrates the strong nonlinearities present in the system. Fig. 5.8(b) displays the time averaged nondimensional axial electroosmotic velocity across the cross section of the nanochannel for different α to further illustrate the decrease in the time averaged axial electroosmotic velocity under large α ($\alpha = 20$). However, minimal variations in the time averaged axial electroosmotic velocity compared to the DC velocity are observed under small amplitude perturbations ($\alpha = 0.2$). Fig. 5.9(a) shows the ratio of the time
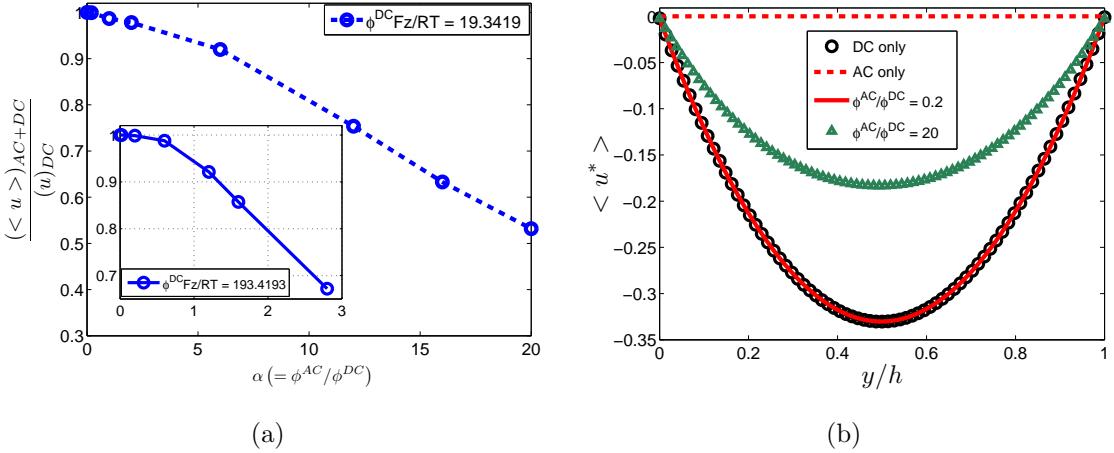

(a)

(b)

Figure 5.8: Numerically calculated velocities (averaged over one time period) measured at the center of the nanochannel ($x/L_0 = 1$) at a fixed $St = 4.65$, $\beta = 0.0049$, $\sigma^* = -109.227$ and $\phi^{DC}Fz/RT = 19.3419$. (a) shows the ratio of the time averaged AC/DC axial electroosmotic velocity to the DC axial electroosmotic velocity as a function of α. The inset of the figure displays the velocity variation with α for a large DC voltage, $\phi^{DC}Fz/RT = 193.419$. (b) depicts the variation of time averaged nondimensional axial electroosmotic velocity across the cross section of the nanochannel for different α. For the AC only case, $\phi^{AC}Fz/RT = 386.84$ and $St = 4.65$. Note: Negative sign indicates flow direction from right to left.

averaged AC/DC axial electroosmotic velocity to the DC axial electroosmotic velocity as a

function of St at a constant amplitude ($\alpha = 16$) and DC voltage ($\phi^{DC}Fz/RT = 19.3419$). The electroosmotic velocity is evaluated at the midpoint of the nanochannel. It can be seen that the time averaged AC/DC axial electroosmotic velocity decreases compared to the DC axial electroosmotic velocity at low St. However, at large St or when the frequency time scale is comparable to the viscous time scale, the time averaged AC/DC axial electroosmotic velocity shows minimal variation compared to the DC axial electroosmotic velocity. These results again can be understood from the fact that the ratio of the time averaged total AC/DC axial electrostatic body force to the total DC axial electrostatic body force exhibits a similar behavior with respect to St and the reason for this variation is discussed in the earlier section. Fig. 5.9(b) displays the time averaged nondimensional axial electroosmotic velocity across the cross section of the nanochannel for different St ($St = 0.233, 4.65$ and 465.12) to further illustrate the aforementioned physics.

(a)

(b)
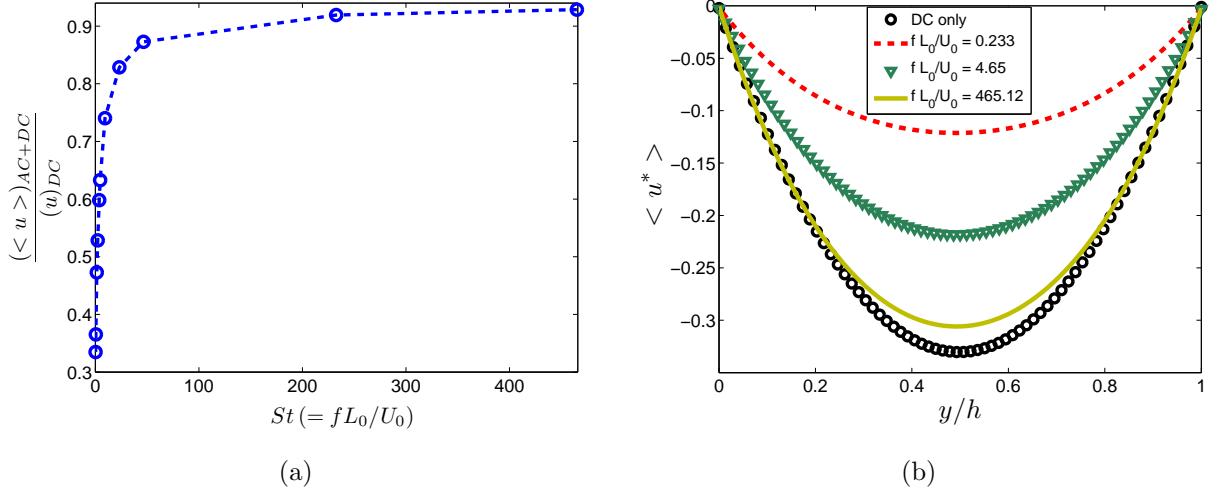
Figure 5.9: Numerically calculated velocities (averaged over one time period) measured at the center of the nanochannel ($x/L_0 = 1$) at a fixed $\alpha = 16$, $\beta = 0.0049$, $\sigma^* = -109.227$ and $\phi^{DC}Fz/RT = 19.3419$. (a) shows the ratio of the time averaged AC/DC axial electroosmotic velocity to the DC axial electroosmotic velocity as a function of St (b) depicts the variation of time averaged nondimensional axial electroosmotic velocity across the cross section of the nanochannel for different St.

Finally, we would also like to briefly point out that, with an application of AC field alone, we observe a symmetric voltage drop and induced pressure gradients at both the interfaces

of micro/nanochannel (see Fig. 5.2(a) and Fig. 5.6(a)). Due to this symmetry, it can be observed from Fig. 5.8(b) that the time averaged axial velocity across the nanochannel is zero and as expected there is no net fluid flow inside the nanochannel.

5.3.4 EDL and nanochannel wall surface charge effects on electrokinetic transport

In all the aforementioned results, in order to understand the effect of combined AC/DC electric fields on the electrokinetic transport under thick EDL regimes, a low ionic concentration of about $1\,mM$ was considered. Under thick electrical double layer regime the nanochannel behaves as an ion$-$selective membrane, i.e., there is a predominant transport of counterions inside the nanochannel. Along with the bulk ionic concentration, several numerical and experimental studies in the recent past have observed the ion$-$selectivity of the nanochannel to depend on the nanochannel wall surface charge density as well [48, 49, 11]. We extend our study and provide additional numerical results to explain the effect of combined AC/DC electric fields on the electrokinetic transport for different system parameters using dimensionless electrical double layer thickness ($\beta = \lambda_D/L_0$) and normalized wall surface charge density of the nanochannel (σ^*). Fig. 5.10 displays the ratio of the time averaged AC/DC axial electroosmotic velocity to the DC axial electroosmotic velocity as a function of St for different nondimensional EDL thickness (β). Here, β is varied by changing the bulk ionic concentration (c_0) of the electrolyte. To understand the frequency effects, the amplitude ($\alpha = 6$) and DC voltage ($\phi^{DC}Fz/RT = 19.3419$) are kept constant and the velocities are evaluated at the midpoint of the nanochannel. It is observed that the voltage gradients and the dual concentration polarization space charge regions (near both the interfaces of micro/nanochannel) predominantly observed at low St increase as the EDL thickness increases resulting in significant decrease in the time averaged AC/DC axial electroosmotic velocity compared to the DC axial electroosmotic velocity. However, when the concentration

of the electrolyte increases i.e., as the nondimensional EDL thickness (β) reduces and the ion$-$selectivity of the nanochannel decreases, the polarization and nonlinear effects under combined AC/DC electric fields decrease and the time averaged AC/DC axial electroosmotic velocity approaches the DC axial electroosmotic velocity indicating minimal AC dependence on the electrokinetic transport.
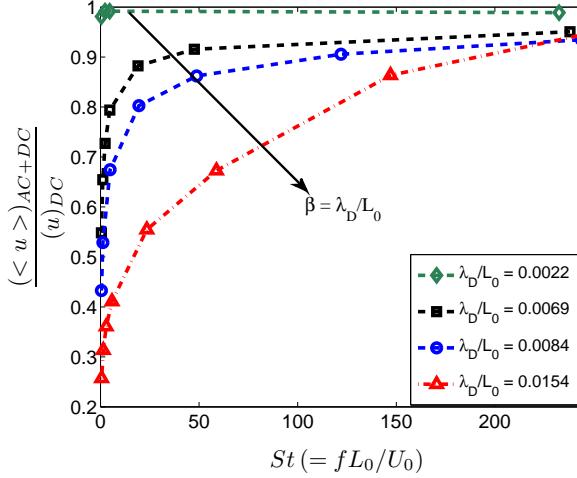

Figure 5.10: Effect of the dimensionless EDL thickness ($\beta = \lambda_D/L_0$) and St on the ratio of the time averaged AC/DC axial electroosmotic velocity to the DC axial electroosmotic velocity. The velocity is measured at the center of the nanochannel ($x/L_0 = 1$) at a fixed $\alpha = 6$, $\sigma^* = -109.227$ and $\phi^{DC}Fz/RT = 19.3419$. β is varied by changing the bulk ionic concentration (c_0) of the electrolyte.

Along with the concentration, as discussed before, the nanochannel wall surface charge density also plays a prominent role in controlling the ion$-$selectivity of the nanochannel. Fig. 5.11 shows the ratio of the time averaged AC/DC axial electroosmotic velocity to the DC axial electroosmotic velocity as a function of St for different normalized nanochannel wall surface charge density (σ^*). Here the amplitude ($\alpha = 6$) and DC voltage ($\phi^{DC}Fz/RT = 19.3419$) are kept constant. It is observed that at large nanochannel wall surface charge density, the channel essentially behaves as an ion$-$selective membrane. As expected, a higher ion$-$selectivity of the nanochannel leads to stronger polarization and nonlinear effects at low St resulting in significant decrease in the time averaged AC/DC axial electroosmotic velocity compared to the DC axial electroosmotic velocity. Furthermore,

47

the results are consistent with our previous arguments that the AC fields have minimal dependence on the electrokinetic transport as the ion−selectivity of the nanochannel decreases which is achieved in this case by reducing the nanochannel wall surface charge density (σ^*). We would also like to highlight that the scaling physics with respect to α is consistent with our previous observations for cases of higher EDL thickness and larger σ^*. From the aforementioned results, we conclude that the ion−selectivity of the nanochannel plays an important role in controlling the concentration polarization effects and electrokinetic transport in micro/nanofluidic interface devices under combined AC/DC electric fields.
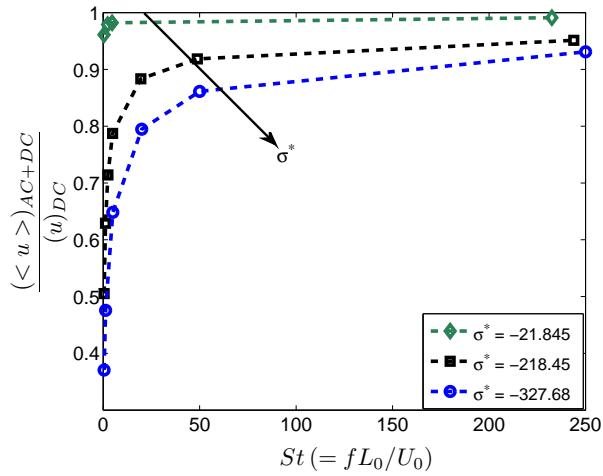

Figure 5.11: Effect of the normalized surface charge density (σ^*) and St on the ratio of the time averaged AC/DC axial electroosmotic velocity to the DC axial electroosmotic velocity. The velocity is measured at the center of the nanochannel ($x/L_0 = 1$) at a fixed $\alpha = 6$, $\beta = 0.0049$ and $\phi^{DC}Fz/RT = 19.3419$.

5.3.5 Side wall reservoir surface charge effects on electrokinetic transport

As mentioned earlier, we perform additional numerical analysis to investigate the effect of side wall reservoir surface charges (σ_w) on the electrokinetic transport under combined AC/DC electric fields. The tests are carried out for different reservoir side wall surface charge densities, i.e., σ_w/σ_{ch} ranges from -2 to 2 at a constant nanochannel wall surface

charge density, $\sigma^* = -109.227$ and $\beta = 0.0049$. The amplitude ($\alpha = 6$), frequency ($St = 4.65$) and DC voltage ($\phi^{DC} Fz/RT = 19.3419$) are also kept constant. As expected, it is observed that the introduction of heterogeneous surface charge at the channel entrance (i.e., if the surface charge polarity on the nanochannel walls (σ_{ch}) is opposite to the reservoir side walls (σ_w)) leads to larger voltage gradients and higher polarization effects at both the interfaces compared to the homogeneous system under the same AC fields (see Fig. 5.12(a)). These polarization effects in turn result in a further decrease in the time averaged axial AC/DC electroosmotic velocity inside the nanochannel. For instance, we observe about

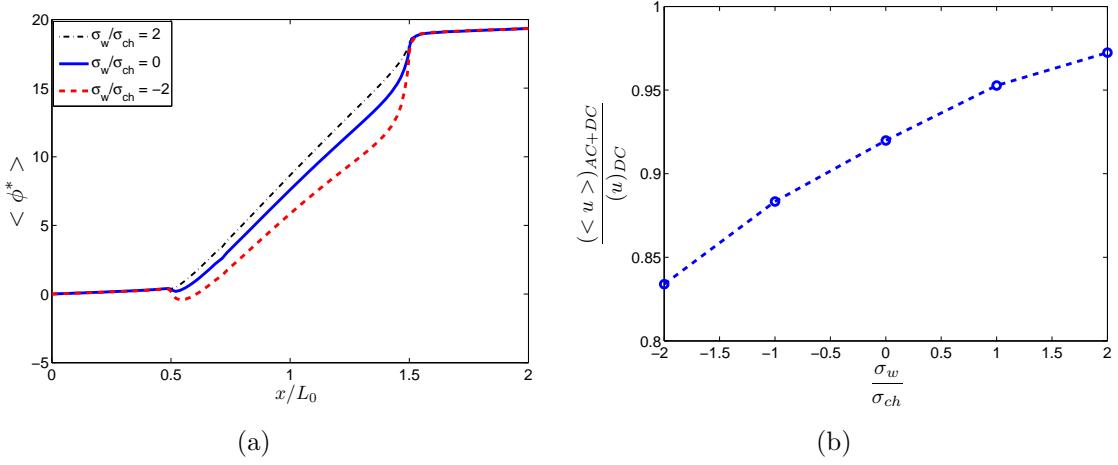(a)   (b)

Figure 5.12: Effect of reservoir side wall surface charge density on the electrokinetic transport. (a) Numerical results of the time averaged nondimensional axial potential distribution for different σ_w/σ_{ch} ($\sigma^* = -109.227$) (b) Ratio of the time averaged AC/DC axial electroosmotic velocity to the DC axial electroosmotic velocity as a function of σ_w/σ_{ch}. The velocity is measured at the center of the nanochannel ($x/L_0 = 1$). In all these cases $\alpha = 6$, $St = 4.65$, $\beta = 0.0049$ and $\phi^{DC} Fz/RT = 19.3419$.

10 % decrease in the time averaged axial electroosmotic velocity under the same AC/DC electric field for a heterogeneous case ($\sigma_w/\sigma_{ch} = -2$) compared to the neutral side wall case (see Fig. 5.12(b)).Although the heterogeneous surface charge distribution at the channel entrance leads to additional polarization effects, we understand that the nanochannel wall surface charge density and the ionic concentration of the electrolyte (i.e., the ion-selectivity of the nanochannel) play a more important role in controlling the concentration polarization

effects and electrokinetic transport in micro/nanofluidic interface devices under combined AC/DC electric fields.

5.4   Conclusions

In this chapter, the effect of combined AC and DC electric fields on the electrokinetic transport and other hydrodynamic properties are investigated in micro/nanofluidic interface devices. Many anomalous and counter−intuitive observations on the electrokinetic transport under different AC/DC electric fields and the underlying physics behind these observations are discussed. For a highly ion−selective nanochannel, strong nonlinear potential distribution and dual concentration polarization space charges at both the interface regions of micro/nanochannel are observed at AC amplitudes greater than the DC field and at low St. The large voltage gradients and the polarization space charges developed near both the interfaces result in significant changes in the electrostatic body force and in the electroosmotic velocity compared to the DC case. The ion−selectivity of the nanochannel is found to play an important role in controlling the concentration polarization effects and electrokinetic transport in micro/nanofluidic interface devices under combined AC/DC electric fields. We believe that understanding of nonlinear transport physics at these interfaces can lead to novel design of micro/nanofluidic interconnect devices. A brief discussion highlighting the importance of AC/DC fields in an enzymatic reaction kinetics is provided in the next chapter.

Chapter 6

AC/DC applications in reaction kinetics

6.1 Introduction

The confinement effects of nanofluidic channels led to many advancements in reaction kinetics. Dai et al. [68] and Dunn et al. [69] showed that reaction between a substrate in solution and a surface−immobilized reagent in a confined nanopore would result in a higher wall collision frequency, causing an increase in the molecular interactions and resulting in higher probability of reactions inside the channel. Experiments by Wang et al. [70] revealed that the higher confinement of reactants inside nanochannels leads to differences in the chemical reactivity as compared to microchannels. In all these studies, the reactants were driven into the channel using DC electric fields. With the understanding of the effects of combined AC/DC fields on the electrokinetic transport inside the nanochannel, a novel technique to increase the product concentration of an enzymatic reaction was investigated using these electric fields. The influence of AC fields on enzyme−catalyzed oxidation of Amplex Red (AR) to Resoruffin (RES) by Hydrogen Peroxide (H_2O_2) in the presence of a Horseradish Peroxidase (HRP) catalyst immobilized on the nanofluidic surface (as considered in the experiments of Wang et al [70]) was numerically investigated. Nanofluidic channels, with higher surface area compared to the microchannels, can result in a higher yield of the products. From numerical simulations using coupled Poisson, Nernst−Planck with reaction kinetics, and incompressible Navier-Stokes equations, the effect of confinement and nanochannel wall surface charge density on the reaction kinetics is investigated. The enzymatic reactions of the form,

$$AR + H_2O_2 + [HRP] \overset{k_T}{\Rightarrow} RES + [HRP] \tag{6.1}$$
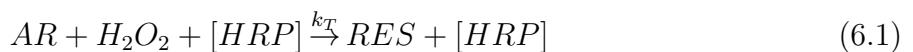
is considered, where the reactants AR and H_2O_2 are Amplex Red and Hydrogen Peroxide respectively, while resoruffin (RES) is the product formed during this reaction. Horseradish Peroxidase (HRP) is the catalyst immobilized on the nanofluidic surface, K_T is the association constant.

6.2   Kinetics model

The spatio−temporal distribution of the reactants and the product (RES) is given by considering the Nernst−Planck and the reaction kinetics equations.

$$\frac{\partial [AR]}{\partial t} = -\nabla \cdot \mathbf{\Gamma}_{AR} - k_T[AR][H_2O_2] \tag{6.2}$$

$$\frac{\partial [H_2O_2]}{\partial t} = -\nabla \cdot \mathbf{\Gamma}_{H_2O_2} - k_T[AR][H_2O_2] \tag{6.3}$$

$$\frac{\partial [RES]}{\partial t} = -\nabla \cdot \mathbf{\Gamma}_{RES} + k_T[AR][H_2O_2] \tag{6.4}$$

where, $\mathbf{\Gamma}_{AR}$, $\mathbf{\Gamma}_{H_2O_2}$ and $\mathbf{\Gamma}_{RES}$ are the total fluxes of the reactants $[AR]$, $[H_2O_2]$ and the product resoruffin $[RES]$, respectively. The flux is obtained by solving the coupled Poisson−Nernst−Planck along with the Navier−Stokes equations as discussed in the previous chapters.

6.3   Simulation model and Boundary conditions

The simulations were carried out using a rectangular nanochannel of length $5\,\mu m$ and varying heights (h) ($10\,nm - 250\,nm$) connected to two reservoirs ($1\,\mu m$ by $1\,\mu m$ cross section) on either side of the channel as shown in Fig. 6.1. In the present study the channels are assumed to be filled with 1mM buffer solution of KH_2PO_4. The reactants and the buffer solution are electrically driven into the channel. The concentration of the reactants and all the other simulation parameters are summarized in Table 6.1. The walls of the nanochannel are positively charged. Similar boundary conditions discussed elaborately in previous chapters
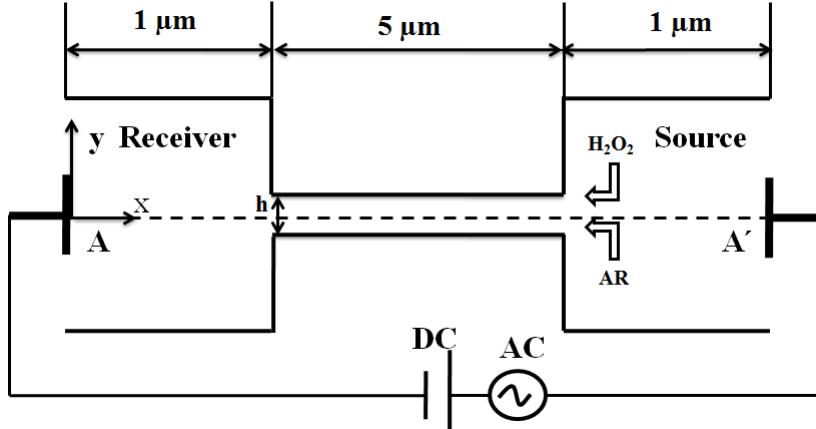
Figure 6.1: Simulation set−up (not drawn to scale), consisting of a nanochannel of height (h) connected to two reservoirs of 1 μm × 1 μm cross−section. The reactants AR and H_2O_2 are electrically driven from the source reservoir, while the enzyme HRP is immobilized on the nanochannel walls.

are applied in the present case. The additional boundary condition is that the flux of each reactant and product species are assumed to be zero on both the micro and nanofluidic channel walls.

6.4 Results and Discussion

The effect of confinement on the rate of product formation is investigated for both DC and AC fields. From Fig. 6.2(a), we observe no significant change in the product concentration as the channel height decreases from 250 nm to 100 nm, while a further reduction in the height leads to a nonlinear increase in the product concentration illustrating the nonlinear dependence on confinement. At low channel heights, as the EDL thickness becomes comparable to the channel height, the concentration of the incoming Amplex Red increases as given by,

$$[AR] \propto \frac{2\sigma_{ch}}{h \, N_A \, e} \tag{6.5}$$

where N_A is the Avogadro number and e is the charge of an electron. As the reaction occurs at the channel walls, the increase in the reactant concentration leads to an increase in the

Table 6.1: Parameters used in the simulation study

S.No	Parameter	Value
1.	Concentration of Amplex Red [AR]	0.010 mM
2.	Concentration of H_2O_2	0.050 mM
3.	Concentration of [HRP] enzyme	1 mM
4.	Diffusivity of [AR]	$1 \times 10^{-9} m^2/s$
5.	Diffusivity of H_2O_2 = Diffusivity of Complex	$1 \times 10^{-9} m^2/s$
6.	Diffusivity of K^+	$1.96 \times 10^{-9} m^2/s$
7.	Diffusivity of $H_2PO_4^-$	$0.87 \times 10^{-9} m^2/s$
8.	K_T - association rate constant	$1.0 \times 10^{-3}/\mu M s$
9.	σ_{ch} - Surface Charge	$0.1\ mC/m^2 - 1.5\ mC/m^2$
10.	h, height of the nanochannel	$10\ nm - 100\ nm$

product formation, thus signifying the importance of confinement and nanoscale environment. With the application of AC field, it was observed that the resoruffin concentration for a channel height of $h = 10\ nm$ increased by 18%. We then investigate the effect of nanochan-
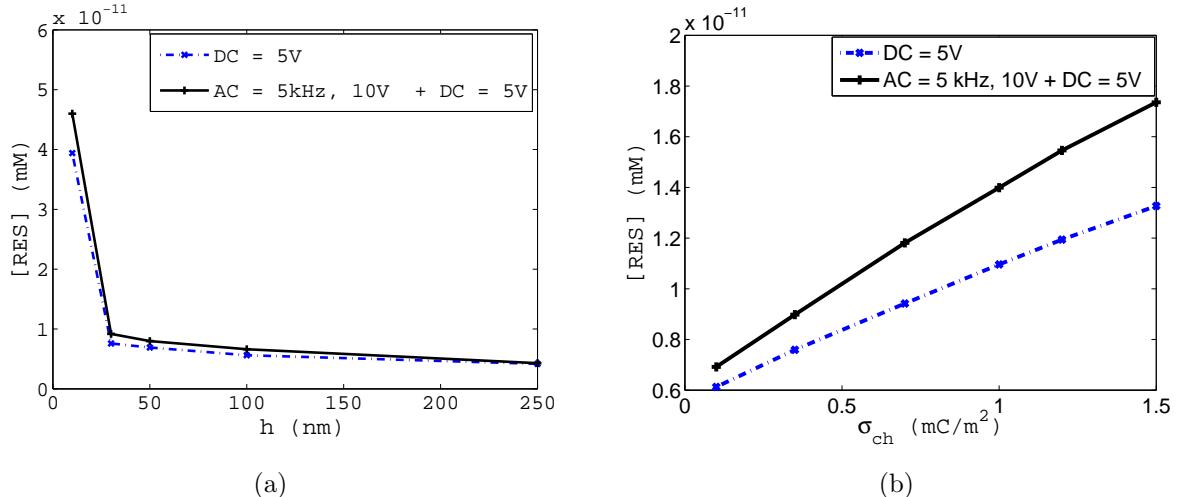

(a)

(b)

Figure 6.2: Confinement and surface charge density effects on reaction kinetics when DC= $5\ V$ and AC= $5\ kHz$ and $10\ V$. (a) Variation of product concentration with channel height. (b) Variation of product concentration with surface charge density

nel wall surface charge density (σ_{ch}) on the product concentration for a fixed channel height of 30 nm. As the surface charge density is increased, the concentration of resorufin increased due to an increase in the concentration of Amplex Red near the charged surface (see Equation (6.5)). Application of an AC field resulted in 30% higher product formation, as shown in Fig. 6.2(b), suggesting a novel approach to enhance the reaction rates in micro and nanofluidic devices. The increase in the product concentration inside the nanochannel is primarily due to an increase in the residence time of the reactant species as the convective fluid velocity of the reactant inside the nanochannel can be controlled by applying the combined AC and DC fields as discussed in the previous chapter. Thus, along with offering interesting fundamental physics in confined systems, the application of combined AC and DC fields also paves way for many novel applications in micro/nanofluidic interconnect devices.

6.5 Conclusions

We propose a novel technique to increase the product concentration of enzymatic reactions inside the nanochannel using combined AC and DC electric fields. The combined electric fields control the convective fluid velocity inside the nanochannel thereby controlling the residence time of the reactant species. Along with the electric fields, the product concentration was also found to depend on the channel confinement and its surface charge density.

Chapter 7

Conclusion and Outlook

In summary, the primary objective of the present thesis work was to investigate the effect of electric fields on the electrokinetic transport in micro/nanofluidic interface devices. Although several studies in the past have highlighted the transport phenomenon under the action of steady DC electric fields, this thesis aimed to understand the effects of electrokinetic transport under combined AC and DC electric fields.

We understood that the integration of micro and nanofluidic channels lead to many complex concentration polarization physics like the enrichment and depletion effects near the interface regions. The application of stronger DC electric fields induced space charges at the depletion region while maintaining electroneutrality at the enrichment region. The induced space charges under the action of an external electric field resulted in nonlinear electroosmosis with the generation of electrokinetic vortices at these interfaces.

The effect of the combined AC and DC electric fields on the electrokinetic transport and other hydrodynamic properties were investigated in micro/nanofluidic interconnect devices. For a highly ion−selective nanochannel, strong nonlinear potential distribution and dual concentration polarization space charges at both the interface regions of micro/nanochannel are observed at AC amplitudes greater than the DC field and at low St. The large voltage gradients and the polarization space charges developed near both the interfaces result in significant changes in the electrostatic body force, pressure and in the electroosmotic velocity compared to the DC case. Further, the ion−selectivity of the nanochannel is found to play an important role in controlling the concentration polarization effects and electrokinetic transport in micro/nanofluidic interface devices under combined AC/DC electric fields.

The potential application of AC/DC fields in increasing the product concentration in

enzymatic reactions was discussed. The residence time of the reactant species was controlled by controlling the convective fluid velocity using combined AC/DC fields. The influence of channel confinement and its surface charge density on the product concentration was numerically investigated.

From the present work, we believe that understanding of nonlinear transport physics at the interfaces of micro/nanofluidic devices can lead to novel design of these interconnect systems for various practical applications.

References

[1] J. W. Hong and S. R. Quake, "Integrated Nanoliter Systems," *Nature Biotechnology*, vol. 21, pp. 1179–1183, 2003.

[2] S. Prakash, A. Piruska, E. N. Gatimu, P. W. Bohn, J. V. Sweedler, and M. A. Shannon, "Nanofluidics: Systems and Applications," *IEEE Sensors J.*, vol. 8, no. 5, pp. 441–450, 2008.

[3] R. B. Schoch, J. Han, and P. Renaud, "Transport phenomena in nanofluidics," *Rev. Mod. Phys.*, vol. 80, pp. 839–883, 2008.

[4] H.-C. Chang and G. Yossifon, "Understanding electrokinetics at the nanoscale: A perspective," *Biomicrofluidics*, vol. 3, p. 012001, 2009.

[5] A. Manz, N. Graber, and H. M. Widmer, "Miniaturized total chemical analysis systems: A novel concept for chemical sensing," *Sens. Actuators B*, vol. 1, pp. 244–248, 1990.

[6] P. C. Simpson, D. Roach, A. T. Woolley, T. Thorsen, R. Johnston, G. F. Sensabaugh, and R. A. Mathies, "High−throughput genetic analysis using microfabricated 96−sample capillary array electrophoresis microplates," *Proc. Natl. Acad. Sci. USA*, vol. 95, pp. 2256–2261, 1998.

[7] A. Hibara, T. Saito, H.-B. Kim, M. Tokeshi, T. Ooi, M. Nakao, and T. Kitamori, "Nanochannels on a fused−silica microchip and liquid properties investigation by time−resolved fluorescence measurements," *Anal. Chem.*, vol. 74, pp. 6170–6176, 2002.

[8] J. O. Tegenfeldt, C. Prinz, H. Cao, R. L. Huang, R. H. Austin, S. Y. Chou, E. C. Cox, and J. C. Sturm, "Micro− and nanofluidics for DNA analysis," *Anal. Bioanal. Chem.*, vol. 378, pp. 1678–1692, 2004.

[9] A. L. Garcia, D. N. P. L. K. Ista, M. J. O'Brien, P. Bisong, A. A. Mammoli, S. R. J. Brueck, and G. P. Lopez, "Electrokinetic molecular separation in nanoscale fluidic channels," *Lab Chip*, vol. 5, pp. 1271–1276, 2005.

[10] R. Karnik, R. Fan, M. Yue, D. Li, P. Yang, and A. Majumdar, "Electrostatic Control of Ions and Molecules in Nanofluidic Transistors," *Nano Lett.*, vol. 5, pp. 943–948, 2005.

[11] R. B. Schoch, H. van Lintel, and P. Renaud, "Effect of the surface charge on ion transport through nanoslits," *Phys. Fluids*, vol. 17, p. 100604, 2005.

[12] C. Ho, R. Qiao, J. B. Heng, A. Chatterjee, R. J. Timp, N. R. Aluru, and G. Timp, "Electrolytic transport through a synthetic nanometer−diameter pore," *Proc. Natl. Acad. Sci. USA*, vol. 102, pp. 10445–10450, 2005.

[13] J. C. T. Eijkel and A. van den Berg, "Water in micro− and nanofluidics systems described using the water potential," *Lab Chip*, vol. 5, pp. 1202–1209, 2005b.

[14] J. W. Perram, R. J. Hunter, and H. J. L. Wright, "Charge and potential at the oxide/solution interface," *Chem. Phys. Lett.*, vol. 23, pp. 265–269, 1973.

[15] J. T. G. Overbeek, "Electrochemistry of the Double Layer," *Colloid Science*, vol. 1, pp. 115–190, 1952.

[16] D. Li, *Electrokinetics in Microfluidics.* Burlington: Elsevier Academic Press, 2004.

[17] R. J. Hunter, *Zeta Potential in Colloid Science.* London: Academic, 1981.

[18] M. Pribyl, D. Snita, P. Hasal, and M. Marek, "Modeling of electric−field driven transport processes in microdevices for immunoassay," *Chem. Eng. J*, vol. 101, pp. 303–314, 2004.

[19] T. M. Squires and S. R. Quake, "Microfluidics: Fluid physics at the nanoliter scale," *Rev. Mod. Phys.*, vol. 77, pp. 977–1026, 2005.

[20] G. E. Karniadakis, A. Beskok, and N. R. Aluru, *Microflows and Nanoflows: Fundamentals and Simulation.* New York, NY: Springer, 2005.

[21] J. Hahm, *Numerical Simulation of Electrokinetically driven micro flows.* PhD. Dissertation, 2005.

[22] R. F. Probstein, *Physiochemical Hydrodynamics: An Introduction.* New York, NY: John Wiley and Sons, Inc., 1994.

[23] F. F. Reuss *Mem. Soc. Imperiale Naturalistes de Moscow*, vol. 2, p. 327, 1809.

[24] E. Hückel *Physik. Z.*, vol. 25, p. 204, 1924.

[25] F. Helfferich, *Ion Exchange.* New York, NY: Dover Publications, 1995.

[26] T. S. Sørensen, *Surface Chemistry and Electrochemistry of Membranes.* New York, NY: Marcel Dekker, 1999.

[27] F. C. Leinweber and M. Pfafferodt and A. Seidel−Morfenstern and U. Tallarek, "Electrokinetic Effects on the Transport of Charged Analytes in Biporous Media with Discrete Ion−Permselective Regions," *Anal. Chem.*, vol. 77, pp. 5839–5850, 2005.

[28] H. Daiguji and P. Yang and A. Majumdar, "Ion transport in nanofluidic channels," *Nano Lett.*, vol. 4, pp. 137–142, 2004.

[29] H. Daiguji, P. Yang, A. J. Szeri, and A. Majumdar, "Electrochemomechanical Energy Conversion in Nanofluidic Channels," *Nano Lett.*, vol. 4, pp. 2315–2321, 2004.

[30] X. Jin, S. Joseph, E. N. Gatimu, P. W. Bohn, and N. R. Aluru, "Induced electrokinetic transport in micro−nanofluidic interconnect devices," *Langmuir*, vol. 23, pp. 13209–13222, 2007.

[31] A. Fulinski, I. D. Kosinska, and Z. Siwy, "On the validity of continuous modelling of ion transport through nanochannels," *Europhys. Lett.*, vol. 67, pp. 683–689, 2004.

[32] R. Qiao and N. R. Aluru, "Ion concentrations and velocity profiles in nanochannel electroosmotic flows," *J. Chem. Phys.*, vol. 118, pp. 4692–4701, 2003.

[33] R. D. Groot and P. B. Warren, "Dissipative particle dynamics: Bridging the gap between atomistic and mesoscopic simulation," *J. Chem. Phys*, vol. 107, pp. 4423–4435, 1997.

[34] R. H. Nilson and S. K. Griffiths, "Influence of atomistic physics on electro−osmotic flow: An analysis based on density functional theory," *J. Chem. Phys.*, vol. 125, p. 164510, 2006.

[35] A. V. Raghunathan, J. H. Park, and N. R. Aluru, "Interatomic potential−based semi-classical theory for Lennard−Jones fluids," *J. Chem. Phys*, vol. 127, p. 174701, 2007.

[36] T. Sanghi and N. R. Aluru, "A transferable coarse−grained potential to study the structure of confined, supercritical Lennard−Jones fluids," *J. Chem. Phys*, vol. 132, p. 044703, 2010.

[37] R. Gross and J. Osterle, "Membrane Transport Characteristics of Ultrafine Capillaries," *J. Chem. Phys.*, vol. 49, pp. 228–234, 1968.

[38] X.-L. Wang, T. Tsuru, S.-I. Nakao, and S. Kimura, "Electrolyte transport through nanofiltration membranes by the space−charge model and the comparison with Teorell−Meyer−Sievers model," *J. Membr. Sci.*, vol. 103, pp. 117–133, 1995.

[39] E. H. Cwirko and R. G. Carbonell, "Transport of electrolytes in charged pores: Analysis using the method of spatial averaging," *J. Colloid Interface Sci.*, vol. 129, pp. 513–531, 1989.

[40] S. Basu and M. M. Sharma, "An improved space−charge model for flow through charged microporous membranes," *J. Membr. Sci.*, vol. 124, pp. 77–91, 1997.

[41] C. C. Chang and R. J. Yang, "Electrokinetic energy conversion in micrometer−length nanofluidic channels," *Microfluid. Nanofluid.*, vol. 9, pp. 225–241, 2010.

[42] http://www.openfoam.com/.

[43] H. K. Versteeg and W. Malalasekra, *An Introduction to Computational Fluid Dynamics: The Finite Volume Method.* 2nd Edition, Pearson Education Ltd., Essex, 2007.

[44] J. D. Anderson, *Computational Fluid Dynamics: The Basics with Applications*. McGraw Hill, 1995.

[45] E. F. Toro, *Riemann Solvers and Numerical Methods for Fluid Dynamics*. Springer−Verlag, 1999.

[46] Y. Wang, K. Pant, Z. Chen, G. Wang, W. F. Diffey, P. Ashley, and S. Sundaram, "Numerical analysis of electrokinetic transport in micro−nanofluidic interconnect pre-concentrator in hydrodynamic flow," *Microfluid. Nanofluid.*, vol. 7, pp. 683–696, 2009.

[47] Q. Pu, J. Yun, H. Temkin, and S. Liu, "Ion-enrichment and ion-depletion effect of nanochannel structures," *Nano Lett.*, vol. 4, pp. 1099–1103, 2004.

[48] A. Mani, T. A. Zangle, and J. G. Santiago, "On the propagation of concentration polarization from microchannel−nanochannel interfaces. Part I. Analytical model and characteristic analysis," *Langmuir*, vol. 25, pp. 3898–3908, 2009.

[49] T. A. Zangle, A. Mani, and J. G. Santiago, "On the propagation of concentration polarization from microchannel−nanochannel interfaces. Part II. Numerical and experimental study," *Langmuir*, vol. 25, pp. 3909–3916, 2009.

[50] I. Rubinstein, *Electrodiffusion of ions*. SIAM, Philadelphia, 1990.

[51] G. Yossifon, P. Mushenheim, Y. C. Chang, and H.-C. Chang, "Nonlinear Current−Voltage Characteristics of Nano−Channels," *Phys. Rev. E*, vol. 79, p. 046305, 2009.

[52] S. J. Kim, Y.-C. Wang, J. H. Lee, H. Jang, and J. Han, "Concentration polarization and nonlinear electrokinetic flow near a nanofluidic channel," *Phys. Rev. Lett.*, vol. 99, p. 044501, 2007.

[53] G. Yossifon and H.-C. Chang, "Selection of Non−Equilibrium Over−Limiting Currents: Universal Depletion Layer Formation Dynamics and Vortex Instability," *Phys. Rev. Lett.*, vol. 101, p. 254501, 2008.

[54] A. Höltzel and U. Tallarek, "Ionic conductance of nanopores in microscale analysis systems: Where microfluidics meets nanofluidics," *J. Sep. Sci.*, vol. 30, pp. 1398–1419, 2007.

[55] P. K. Wong, C.-Y. Chen, T.-H. Wang, and C.-M. Ho, "Electrokinetic bioprocessor for concentrating cells and molecules," *Anal. Chem.*, vol. 76, pp. 6908–6914, 2004.

[56] M. H. Oddy, J. G. Santiago, and J. C. Mikkelsen, "Electrokinetic Instability Micromixing," *Anal. Chem.*, vol. 73, pp. 5822–5832, 2001.

[57] G. H. Tang, Z. Li, J. K. Wang, Y. L. He, and W. Q. Tao, "Electroosmotic flow and mixing in microchannels with the lattice Boltzmann method," *J. Appl. Phys.*, vol. 100, p. 094908, 2006.

[58] A. Ajdari, "Pumping liquids using asymmetric electrode arrays," *Phys. Rev. E*, vol. 61, p. R45, 2000.

[59] A. B. D. Brown, C. G. Smith, and A. R. Rennie, "Pumping of water with ac electric fields applied to asymmetric pairs of microelectrodes," *Phys. Rev. E*, vol. 63, p. 016305, 2001.

[60] A. Ramos, A. González, A. Castellanos, N. G. Green, and H. Morgan, "Pumping of liquids with ac voltages applied to asymmetric pairs of microelectrodes," *Phys. Rev. E*, vol. 67, p. 056302, 2003.

[61] P. Dutta and A. Beskok, "Analytical Solution of Time Periodic Electroosmotic Flows: Analogies to Stokes' Second Problem," *Anal. Chem.*, vol. 73, pp. 5097–5102, 2001.

[62] D. Erickson and D. Li, "Analysis of Alternating Current Electroosmotic Flows in a Rectangular Microchannel," *Langmuir*, vol. 19, pp. 5421–5430, 2003.

[63] J. K. Chen, W. J. Luo, and R. J. Yang, "Electroosmotic Flow Driven by DC and AC Electric Fields in Curved Microchannels," *Jpn. J. Appl. Phys.*, vol. 45, pp. 7983–7990, 2006.

[64] L. H. Olesen, M. Z. Bazant, and H. Bruus, "Strongly nonlinear dynamics of electrolytes under large AC voltages," *Phys. Rev. E*, vol. 82, p. 011501, 2010.

[65] S. Bhattacharyya and A. K. Nayak, "Time periodic electro−osmotic transport in a charged micro/nanochannel," *Colloid Surf. A: Physicochem. Eng. Aspects*, vol. 325, pp. 152–159, 2008.

[66] Y.-C. Wang, A. L. Stevens, and J. Han, "Million−fold preconcentration of Proteins and Peptides by Nanofluidic Filter," *Anal. Chem.*, vol. 77, pp. 4293–4299, 2005.

[67] S. S. Dukhin and V. N. Shilov, "Theory of static polarization of the diffuse part of the thin electric double layer of spherical particles," *Kolloid. Zh.*, vol. 31, pp. 706–713, 1969.

[68] J. H. Dai, G. L. Baker, and M. L. Bruening, "Use of Porous Membranes Modified with Polyelectrolyte Multilayers as Substrates for Protein Arrays with Low Nonspecific Adsorption," *Anal. Chem.*, vol. 78, pp. 135–140, 2006.

[69] J. D. Dunn, J. T. Watson, and M. L. Bruening, "Detection of phosphopeptides using Fe(III)−nitrilotriacetate complexes immobilized on a MALDI plate," *Anal. Chem.*, vol. 78, pp. 1574–1580, 2006.

[70] Z. Wang, T. L. King, S. P. Branagan, and P. W. Bohn, "Enzymatic activity of surface−immobilized horseradish peroxidase confined to micrometer−nanometer−scale structures in nanocapillary array membranes," *Analyst*, vol. 134, pp. 851–859, 2009.